Geochemistry and petrogenetic implications of a Late Devonian mafic–ultramafic intrusion at the southern margin of the Central Asian Orogenic Belt

Wei Xie [a,b], Xie-Yan Song [a,*], Yu-Feng Deng [a], Yu-Shan Wang [c], Duo-Heng Ba [c], Wen-Qin Zheng [a], Xiao-Biao Li [a]

[a] State Key Laboratory of Ore Deposit Geochemistry, Institute of Geochemistry, Chinese Academy of Sciences, Guiyang 550002, PR China
[b] Graduate University of Chinese Academy of Sciences, Beijing 100049, PR China
[c] Jinchuan Group, Ltd., Jinchang, Gansu 737100, PR China

ABSTRACT

The Heishan mafic–ultramafic intrusion was emplaced into Neoproterozoic metamorphic strata in the eastern Beishan Fold Belt at the southern margin of the Central Asian Orogenic Belt. The dominant rocks of the intrusion are harzburgite and lherzolite. Olivine gabbro-norite and gabbro dyke occur only along the southern margins of the intrusion. The rocks of the Heishan intrusion are characterized by enrichments of large ion lithophile elements, strong negative Nb (Ta) anomalies and positive K and Pb anomalies. These features are perfectly consistent with those of the Devonian volcanics in the Beishan Fold Belt and indicate subduction-related magmatism. The Heishan intrusive rocks have restricted $\varepsilon_{Nd(t)}$ (+0.34 to +3.95) and a large range of $(^{87}Sr/^{86}Sr)_t$ ratios (0.7041 to 0.7087). Their high $(^{207}Pb/^{204}Pb)_t$ (15.55–15.64) and $(^{208}Pb/^{204}Pb)_t$ (37.71–38.29) values are comparable with those of the volcanics along the Pacific margins of the Americas. Zircon ID-TIMS U–Pb age data (356.4±0.6 Ma and 366.6±0.6 Ma) and SHRIMP U–Pb age data (358±5 Ma and 357±4 Ma) indicate that the intrusion was emplaced in the Late Devonian. Our calculations indicate that the parental magma of the Heishan intrusion had a high-Mg basaltic composition with ~11.3 wt.% MgO and ~10.0 wt.% FeO_T. It is proposed that the high-Mg basaltic magma was generated from partial melting of the asthenosphere and mantle wedge triggered by upwelling of asthenosphere due to slab break-off in an active continental margin.

© 2012 Elsevier B.V. All rights reserved.

1. Introduction

Subduction-related calc-alkaline intermediate and acid magmatism is common at active continental margins (Arculus and Powell, 1986; Hawkesworth and Powell, 1980). Basaltic magmas may be generated from melting of upwelling asthenosphere due to slab break-off in subduction zones, such as in the Alps and the Pacific margin of the Americas (e.g., Davies and von Blanckenburg, 1995; Thorkelson, 1996). These basaltic magmas have both MORB- and arc-like elemental and isotopic features because the ascending asthenosphere reacted with mantle wedge (e.g., Astis et al., 2006; Gorring et al., 2003; Keskin, 2003; Miller et al., 2000). Magmatic sulfide mineralization has been found in mafic–ultramafic intrusions in arc settings in the past decades (Maier et al., 2008; Paktunc, 1990; Pina et al., 2006; Tornos et al., 2001). These discoveries reveal an exploration potential for magmatic deposits in tectonic settings other than continental rift zones.

The Central Asian Orogenic Belt (CAOB) is a massive, complex Phanerozoic accretionary collage (Fig. 1a). It is widely accepted that

it grew generally from the north to the south (Dobretsov, 2003; Mossakovsky et al., 1993; Sengör and Natal'in, 1996; Sengör et al., 1993). Although Ordovician–Silurian termination of accretion at the southern CAOB has been proposed (Han et al., 1997; He et al., 1994; Kheraskova et al., 2003; Su et al., 2011; Tang, 1990; Tang and Yan, 1993), recent studies have suggested that the accretionary processes continued up to the Carboniferous–Permian (Laurent-Charvet et al., 2003; Wang et al., 2010; Xiao et al., 2004, 2008, 2010). Permian mafic–ultramafic intrusions have been discovered in the Northern and Central Tianshan (e.g., Huangshan, Tulaergen) and the Beishan Fold Belt (including Pobei, Hongshishan, Bijiashan, Luodong and a few in the Liuyuan area), NW China, at the southern margin of the CAOB (Fig. 1), and dated at 260–290 Ma except Tulaergen (300.5± 3.2 Ma, 357.5±2.5 Ma) and Xiadong mafic–ultramafic complex (Late Carboniferous) (e.g., Ao et al., 2010; Han et al., 2004; Jiang et al., 2006; Li et al., 2006; Qin et al., 2003, 2011; San et al., 2010; Su et al., 2010a,b, 2011, 2012; Tang et al., 2009; Wu et al., 2005; Zhang et al., 2011; Zhou et al., 2004). Published syntheses describing the tectonic setting of these intrusions are controversial. Xiao et al. (2004, 2008) and Han et al. (2010) proposed that these intrusions are subduction-related Alaskan-type intrusions, whereas some of these intrusions have been linked to post-collisional magmatism (e.g., Han et al., 2004; Song and Li, 2009; Zhang et al., 2006, 2009). Others

* Corresponding author at: State Key Laboratory of Ore Deposit Geochemistry; Institute of Geochemistry, Chinese Academy of Sciences; 46th Guanshui Road, Guiyang 550002, PR China. Tel: +86 0851 5895538; fax: +86 0851 5891664.

E-mail address: songxieyan@vip.gyig.ac.cn (X.-Y. Song).
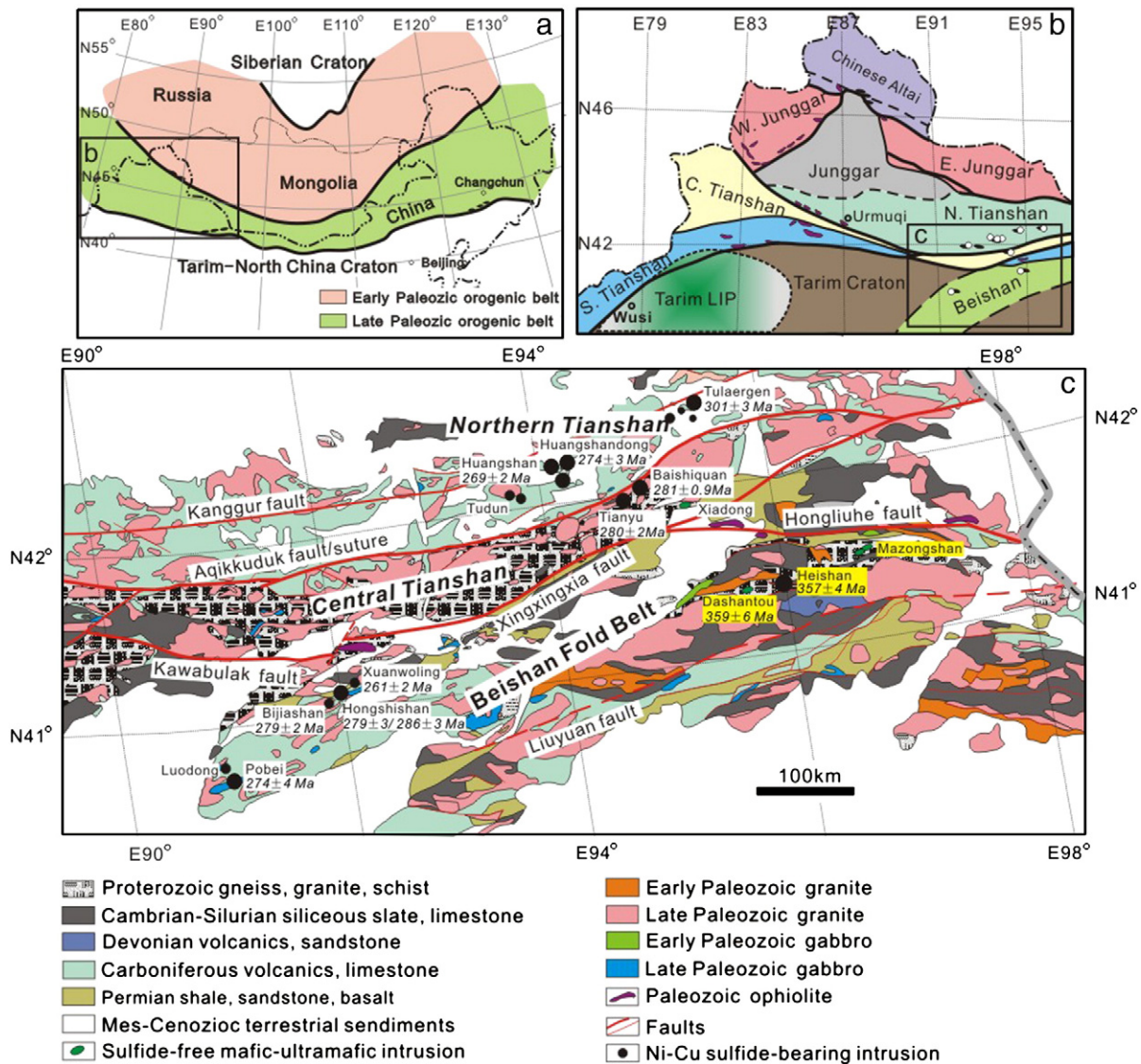
Fig. 1. (a) Schematic geological map of the Central Asian Orogenic Belt; (b) tectonic units of the northern Xinjiang, NW China; (c) simplified geological map of the Beishan Fold Belt. CAOB in (a) is from Song and Li (2009). Simplified geological map of the Beishan Fold Belt in (b) is from BGMRG (1989) and BGMRXUAR (1993).

have argued that these Permian intrusions were produced by a Permian mantle plume (e.g., Pirajno et al., 2008; Qin et al., 2011; Su et al., 2011).

The Heishan mafic–ultramafic intrusion contains an economic magmatic Ni–Cu deposit and is the first one dated at ~357 ± 4 Ma in the east part of the Beishan Fold Belt (Fig. 1c). The age data of the Heishan intrusion suggest that mantle plume is not the prerequisite factor for at least some of the magmatic Ni–Cu deposit hosting mafic–ultramafic intrusions at the southern margin of the CAOB. The purpose of this paper is to constrain the genesis of the Heishan intrusion, and use this information to unravel the tectonic evolution of the southern margin of the CAOB in late Paleozoic. New trace element and Sr–Nd–Pb isotope data lead us to link the intrusion to subduction slab break-off magmatism during the Late Devonian.

2. Regional geology

The Central Asian Orogenic Belt (CAOB) extends >5000 km west to east, and is a complex collage of continental fragments, island arc assemblages, remnants of oceanic crust and continental margins, set between the Siberian Craton to the north and the Tarim–North China Craton to the south (Fig. 1a). It was formed by multiple subduction–

accretion and collision processes from the Neoproterozoic to the Late Paleozoic (Jahn et al., 2000, 2004; Sengör et al., 1993; Windley et al., 2007; Xiao et al., 2004, 2008, 2010). The southern CAOB in northwest China consists, from north to the south, of the Chinese Altai, Junggar, Tianshan domains and Beishan Fold Belt, respectively (Fig. 1b).

The NE–SW trending Beishan Fold Belt is located to northeast of the Tarim block at the southernmost margin of the CAOB (Fig. 1). It is separated from the Tianshan terranes to the northwest by Xingxingxia faults (Fig. 1b, BGMRG, 1989; BGMRXUAR, 1993). The ophiolite along the Hongliuhe fault was crosscut by the undeformed granite with a SHRIMP zircon U–Pb age of 405 ± 5 Ma (Zhang and Guo, 2008) and ophiolite along the Kawabulak fault was formed at 377 ± 2 Ma (Xiao et al., 2008). These ophiolites probably reflect remnants of Paleozoic southern Tianshan oceanic plate (e.g., Guo et al., 2002, 2006; Xiao et al., 2008; Zhang and Guo, 2008). Like the Tarim block and Central Tianshan terrane, the Beishan Fold Belt has a Neoproterozoic crystalline basement, which is uncomfortably overlain by Paleozoic sequences (Fig. 1c, BGMRG, 1989; BGMRXUAR, 1993). The Paleozoic strata include the Cambrian–Silurian shallow marine clastics and volcanic rocks, Devonian–Carboniferous marine clastic–carbonate and arc volcanics, and Permian shallow marine clastics and pillow basalts. The thick Devonian–Carboniferous arc volcanics are dominated by andesites,

rhyolites and minor basalts (BGMRG, 1989; BGMRXUAR, 1993). The Pobei, Hongshishan, Xuanwoling, and Luodong mafic–ultramafic intrusions in the western part of the Beishan Fold Belt have been dated at 260–290 Ma (e.g., Jiang et al., 2006; Li et al., 2006; Qin et al., 2011; Su et al., 2010a,b, 2011), and several intrusions in the Liuyuan area, in the eastern part of the fold belt, were dated at 270–295 Ma (Zhang et al., 2011) (Fig. 1c). Permian transitional alkaline to tholeiitic basalts covering an area of ~250,000 km^2 and related mafic–ultramafic intrusions in the western part of the Tarim block are attributed to a mantle plume (Fig. 1b) (e.g., Carroll et al., 1995; Chen et al., 1997; Li et al., 2008; Yang et al., 2006; Zhang et al., 2008).

3. Petrology of the Heishan intrusion

The oval Heishan mafic–ultramafic intrusion is ~800 m long and ~470 m wide. It is emplaced in the Neoproterozoic metamorphic strata, composed of dolomitic marble and siliceous slate, with interlayers of meta-basalt and -andesite (Fig. 2). The intrusion dips southwest to a depth of more than 800 m according to the exploration drills (Fig. 2b). The dominant rocks of the Heishan intrusion are harzburgite and lherzolite. The harzburgite comprises 40–75 modal % olivine (Ol), 15–40% orthopyroxene (Opx), <10% plagioclase (Pl) and minor hornblende (Hbl) and biotite (Bt). With decreasing Ol and Opx upwards, the harzburgite grades into lherzolite, which consists of 35–60% Ol, 20–30% Opx, 10–25% Cpx (clinopyroxene) and ~10% Hbl and Bt and <5% Pl. Olivine is commonly in granular texture and

Fig. 2. (a) Simplified geological map of the Heishan intrusion; (b) cross section of the prospecting line No. 16 showing the lithological units and sulfide ore bodies.

poikilitically enclosed in granular Opx and interstitial Cpx in these rocks (Fig. 3). Both harzburgite and lherzolite contain minor Cr-spinel, which is generally hosted in Ol. Hornblende and Bt generally fill interstices between Ol and pyroxene, and Hbl may form reaction coronae of Cpx and Opx (Fig. 3c). Olivine gabbro-norite with a thickness of 10–30 m overlies the lherzolite along the southern margins of the intrusion (Fig. 2). It consists of 10–20% Ol, 15–25% Opx, 10–25% Cpx, 20–30% Pl, and 10–20% Hbl and Bt. Textures suggest the following crystallization sequence: Cr-spinel → Ol → Opx → Cpx → Pl → Hbl + Bt in these rocks. Olivine and pyroxenes in these Heishan rocks have been partially altered to serpentine and chlorite (Fig. 3).

Gabbro dykes, with sharp contacts between them, have intruded the harzburgite and lherzolite, and also the olivine gabbro-norite along the southwestern margin of the Heishan intrusion. They contain 20–30% Cpx, 50–65% Pl and ~10% Hbl and are characterized by a diabasic texture at the contact chilled margins.

Lenticular Ni–Cu sulfide ore bodies occur within the harzburgite at the base and lower parts of the intrusion (Fig. 2b). The sulfide ores are generally disseminated; net-textured and semi-massive ores are rare. The two largest ore bodies, No. 1 and No. 4 ore bodies, host ~200 million tons of ores with average grades of 0.6 wt.% Ni and 0.3 wt.% Cu.

In contrast, the Permian Pobei intrusion (~25 km long and ~10 km wide) dated at 274 ± 4 Ma and 278 ± 4 Ma (Jiang et al., 2006; Li et al., 2006) occurring in the western part of the Beishan Fold Belt is composed of gabbroic rocks predominantly. A number of magmatic sulfide-bearing ultramafic bodies occur in the western part of the Pobei intrusion and are composed mainly of wehrlite, which shows sharp contacts with adjacent gabbros (e.g., Mao et al., 2008; Song et al., 2011; Xie et al., 2011).

4. Analytical methods

4.1. Zircon U–Pb dating

The zircons for SHRIMP (Sensitive High Resolution Ion Microprobe) and ID-TIMS (isotope dilution thermal ionization mass spectrometry) U–Pb dating were processed by conventional magnetic and heavy liquid separation methods, and then handpicked out under binocular microscope to select zircon grains for analysis. Approximately 50 kg of gabbro dyke (GHSN-01, GHCN-01, GHCN-02) and olivine gabbro-norite (GHSN-02) of the Heishan intrusion (Fig. 2) were crushed for zircon crystal separation, respectively.

It was provided 50 and 18 zircon crystals from gabbro dyke (GHSN-01) and olivine gabbro-norite (GHSN-02), respectively. Transparent, short, prismatic, euhedral zircon crystals without inclusions (5 zircon grains from GHSN-01 and 2 from GHSN-02) were chosen for ID-TIMS U–Pb dating at the Isotope Research Center based in Tianjin Institute of Geology and Mineral Resources. All analyses were carried out on a VG354 thermal ion mass spectrometer operated in single Daly collector peak hopping mode and were corrected for mass discrimination based on replicate measurement of NBS982. Repeated analysis of a total procedural blank during this study was <0.05 and <0.002 ng for Pb and U, respectively. Data calculation was performed using the Isoplot program of Ludwig (1994). The error ellipses shown on all concordia diagrams and age uncertainties are reported at 2σ. The analytical procedure is similar to that of Krogh (1973) and described in detail by Lu et al. (2003). It should be noted that a ^{208}Pb spike was used in this study.

The zircon grains (GHCN-01 and GHCN-02) were mounted in epoxy, and then polished for cathodoluminescence (CL) observation and SHRIMP analyses. The CL images were taken using a HITACHI S3000-N scanning electron microscope (SEM) and the zircon in situ U–Th–Pb analyses were performed using a SHRIMP II at the Beijing SHRIMP Center, the Institute of Geology, Chinese Academy of Geological Sciences. Analytical procedures follow those of Compston et al. (1992), Williams (1998) and Song et al. (2002). The standard zircons TEM (417 Ma, with variable U-content) (Black et al., 2003) were used
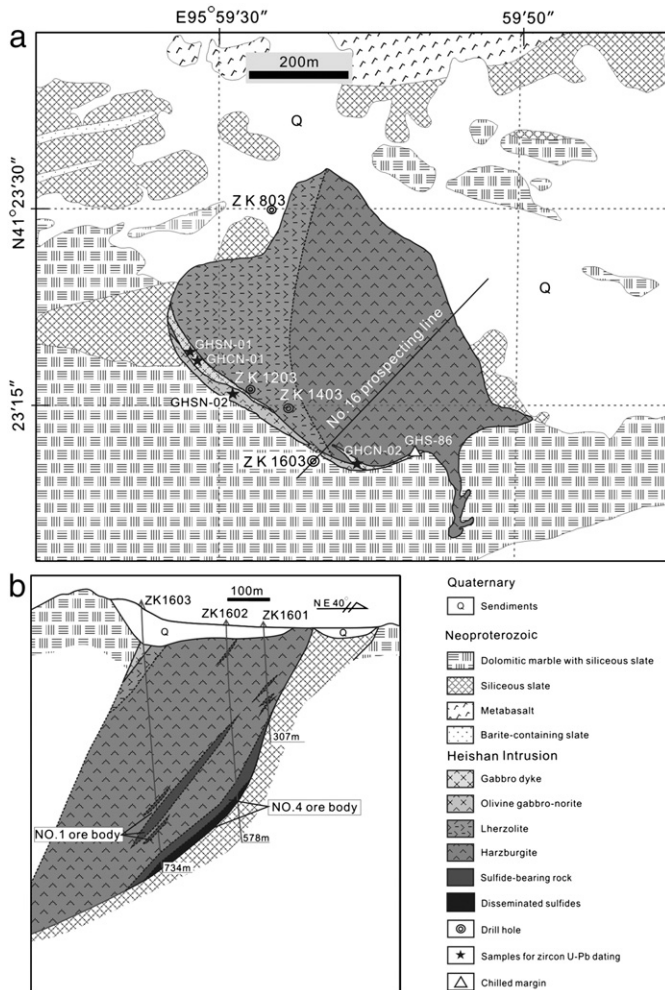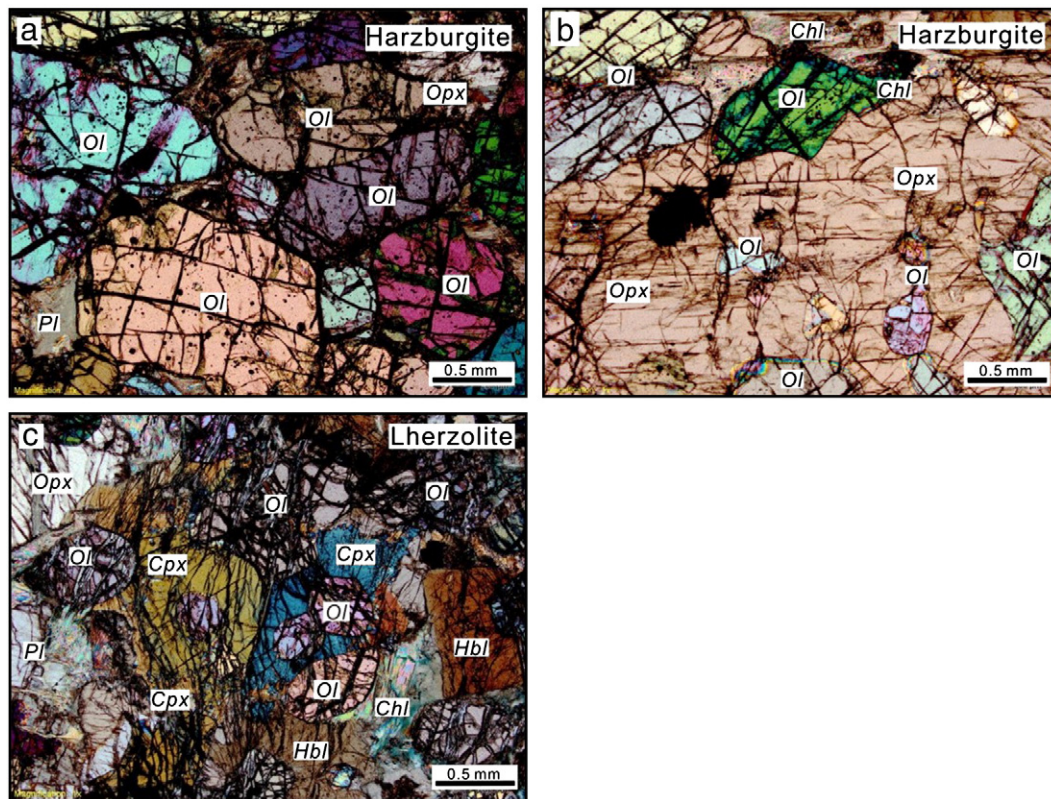
Fig. 3. Photomicrographs in orthogonal light showing typical textures of samples from the Heishan intrusions: (a) olivine granular and netted texture in harzburgite at the base of the Heishan intrusion; (b) olivine poikilitic texture in harzburgite in the mid-upper part of the intrusion; (c) poikilitic texture and hornblende reaction rim texture in lherzolite. Most olivine grains in the samples are partially altered to serpentine and form netted texture. Some pyroxene and plagioclase are partially altered to chlorite and sericite. Ol, olivine; Opx, orthopyroxene; Cpx, clinopyroxene; Pl, plagioclase; Hbl, hornblende; Bt, biotite; Chl, chlorite.

to correct for interelement fractionation, and U, Th and Pb concentrations were determined based on the standard zircons M257 (561.3 Ma, U = 840 ppm) (Nasdala et al., 2008). Data processing was carried out using the SQUID 1.03 and Isoplot/Ex2.49 programs of Ludwig (2001a, b), and the ^{204}Pb-based method of common Pb correction was applied. Uncertainties for each analysis are at 1σ, whereas the weighted mean age is quoted at 2σ.

4.2. Mineral chemistry

Olivine and clinopyroxene from the Heishan sulfide-free rocks of ZK1603 are selected to be determined by wavelength-dispersive X-ray analysis using an EPMA-1600 electron microprobe at the Institute of Geochemistry, Chinese Academy of Sciences. The analytical conditions were beam current of 20 nA, acceleration voltage of 15 kV and a beam size of 10 μm in diameter, and the counting time was 20–40 s for major elements and 40–60 s for minor elements. SPI mineral standards (USA) were used for calibration.

4.3. Major and trace elements

Rock samples were collected from 4 drill cores (ZK803, ZK1203, ZK1403, ZK1603, Fig. 2) and weakly altered outcrops in the Heishan intrusion. Major oxides of the samples containing <3 modal% sulfides were measured using a PANalytical Axios X-ray fluorescence spectrometer (XRF) on fused glass beads at the ALS Chemex (Guangzhou) Co., Ltd. with an analytical uncertainty less than 5%. 0.7 g powder of such samples are mixed completely with flux $Li_2B_4O_7$–$LiBO_2$ and then fused to a glass bead at 1050–1100 °C in an automatic melting instrument. Selected trace elements were determined using a Perkin-Elmer Sciex ELAN DRC-e inductively coupled plasma mass spectrometer (ICP-MS) at the Institute of Geochemistry, Chinese Academy of

Sciences, with analytical uncertainty better than 10%. Samples were digested with 1 ml of HF and 0.5 ml of HNO_3 in screw top PTFE-lined stainless steel bombs at 190 °C for 12 h. The analytical precision is generally better than 1% for elements with concentrations > 200 ppm, and 1–3% when less than 200 ppm. The procedure for the trace elements is described in detail by Qi et al. (2000).

4.4. Sr, Nd, Pd isotopes

Rb–Sr and Sm–Nd isotopic analyses were performed on a TRITON thermal ionization magnetic sector mass spectrometer (TIMS) at the Institute of Geochemistry, Chinese Academy of Sciences. Mass fractionation corrections for Sr and Nd isotopic ratios were based on values of ^{86}Sr/^{88}Sr = 0.1194 and ^{146}Nd/^{144}Nd = 0.7219. Analyses of the NBS-987 Sr standard yielded an ^{86}Sr/^{88}Sr ratio of 0.710255 ± 0.000007(n = 40), whereas analyses of the JNdi-1 Nd standard yielded a ^{146}Nd/^{144}Nd ratio of 0.512096 ± 0.000005(n = 40). Uncertainties in Rb–Sr and Sm–Nd ratios are less than ± 2% and ± 0.5% (relative), respectively. Lead isotopic analyses were performed on an IsoProbeT thermal ionization magnetic sector mass spectrometer (TIMS) at the Beijing Research Institute of Uranium Geology, China. The ^{204}Pb/^{206}Pb, ^{207}Pb/^{206}Pb and ^{208}Pb/^{206}Pb ratios of the NBS981 Pb isotopic standard determined during this study were 0.059003 ± 84 (1σ), 0.91439 ± 17 (1σ) and 2.16441 ± 97 (1σ), respectively. The measured isotope ratios were corrected to 357 Ma based on U, Th and Pb contents determined by ICP-MS.

5. Analytical results

5.1. Zircon U–Pb age

ID-TIMS U–Pb data are listed in Table 1a. Three zircon grains of GHSN-01 plot perfectly on the concordia curve and another two

Table 1a
ID-TIMS U–Pb isotopic data for zircons of GHSN-01 and GHSN-02 from the Heishan intrusion.

Sample features	Concentration				Common	Isotopic atomic ratios					Apparent ages(Ma)		
Grains no.	Color and shape	Weight (μg)	U (ppm)	Pb (ppm)	Pb (ng)	$^{206}Pb/^{204}Pb$	$^{208}Pb/^{206}Pb$	$^{206}Pb/^{238}U$	$^{207}Pb/^{235}U$	$^{207}Pb/^{206}Pb$	$^{206}Pb/^{238}U$	$^{207}Pb/^{235}U$	$^{207}Pb/^{206}Pb$
GHSN-01 gabbro dyke													
1	Light yellow-brown, short prismatic	120	1069	78	0.05	3792	0.4147	0.05672 (10)	0.4197 (11)	0.05367 (10)	355.6 (0.6)	355.8 (0.9)	357.2 (4.3)
2	Light yellow-brown, short prismatic	70	918	67	0.064	2178	0.4112	0.05687 (15)	0.4211 (14)	0.05370 (11)	356.6 (0.9)	356.8 (1.2)	358.6 (4.8)
3	Light yellow-brown, short prismatic	90	1070	77	0.013	14890	0.4086	0.05684 (10)	0.4203 (8)	0.05363 (5)	356.4 (0.6)	356.3 (0.7)	355.6 (2.3)
4	Light yellow-brown, long prismatic	60	1524	117	1.1	1500	0.459	0.05686 (26)	0.4226 (28)	0.05390 (25)	356.5 (1.6)	357.9 (2.4)	367.1 (11)
5	Light yellow-brown, long prismatic	30	1158	91	1.1	623	0.4352	0.05692 (11)	0.423 (27)	0.05389 (32)	356.9 (0.7)	358.2 (2.3)	366.6 (13)
GHSN-02 olivine gabbro-norite													
1	Light purple, short prismatic	20	795	83	0.26	134	0.3894	0.05852 (12)	0.4347 (146)	0.0539 (17)	366.6 (0.8)	366.5 (12)	366 (72)
2	Light purple, irregular granular	40	970	79	0.13	662	0.4505	0.05853 (13)	0.4361 (33)	0.0540 (4)	366.7 (1.0)	367.5 (2.7)	373 (15)

Note: figures in bracket are 2σ absolute errors, for example: 0.05672 (10) represents 0.05672 ± 0.00010 (2σ); error of $^{206}Pb/^{238}U$ age is 2σ; the ratio of $^{206}Pb/^{204}Pb$ has been corrected using the experimental blank.

high-U grains plot slightly away from the concordia curve because of high common Pb (1.1 ng), suggesting that they may have suffered minor Pb loss (Table 1a). Analyses of the five individual zircon crystals form a single age group and yield a mean $^{206}U/^{238}Pb$ age of 356.4 ± 0.6 Ma with a mean square of weighted deviations (MSWD) of 1.81 (Fig. 4a). The two grains of GHSN-02 plot on the concordia curve with the $^{206}Pb/^{238}U$ apparent ages falling in a narrow range from 366.6 to 366.7 Ma, although one zircon has a large 2σ of $^{207}Pb/^{235}U$, probably because of the fluctuation of ^{207}Pb (Fig. 4b). Thus, these results are still very reliable and are taken to reflect the crystallization age of the Heishan rocks. The two zircon grains yielded a weighted mean age of 366.6 ± 0.6 Ma (MSWD = 0.0254) (Fig. 4b). These zircon U–Pb ages indicate that the gabbro dyke formed slightly later than the main Heishan intrusion.

The zircons in gabbro dyke samples GHCN-01 and GHCN-02 exhibit mostly long/short prismatic morphologies and a variety of textures with complex internal structures. The internal complexities of the zircons do not appear to affect the ages obtained from different grains, as all analyses yielded a single age within analytical uncertainties, including cores, rims, high and low U regions, and crystals of different shapes. 20 zircon grains from GHCN-01 and 13 zircon grains from GHCN-02 were analyzed by SHRIMP. These zircons have high U, Th and radiogenic Pb contents of 182–1862 ppm, 140–3177 ppm and 9–89 ppm, respectively, with high Th/U ratios of 0.63–1.78 (Table 1b). GHCN-01 and GHCN-02 yield a mean $^{206}U/^{238}Pb$ age of 358 ± 5 Ma (MSWD = 1.6) and 357 ± 4 Ma (MSWD = 1.04), respectively (Fig. 4c, d). These zircon U–Pb ages indicate that the gabbro dyke formed in the Late Devonian.

5.2. Mineral compositions

Representative olivine compositions from the Heishan sulfide-free ultramafic rocks of ZK1603 are listed in Table 2. The forsterite (Fo) percentages of the olivine range from 80 to 87% in the different rock types. The olivine crystals of the harzburgites contain the highest MgO (43–46 wt.%) and Fo (81.6–86.9%), whereas those of the lherzolites have lower MgO (42–45 wt.%) and Fo (80.5–85.1%).

Clinopyroxene (Cpx) compositions from the Heishan sulfide-free rocks of ZK1603 are listed in Table 3. The enstatite (En) percentages of the Cpx range from 46 to 51% in the different rock types. Only one Cpx grain (En = 49.7) is found in the lherzolite sample GHH-109. The Cpx in the harzburgites and olivine gabbro-norites have similar MgO contents (15.8–17.7 wt.% and 16.5–17.8 wt.%, respectively) and En (46.4–50.7% and 48.6–51.2%), and Al_2O_3 and TiO_2 contents (Table 3).

5.3. Major oxides and trace elements

Representative major and trace element contents of the Heishan rocks are listed in Table 4. In the following plots and discussion, all oxide contents of have been recalculated to 100% in a volatile- and sulfide-free basis.

The Heishan intrusive rocks display regular compositional variations, consistent with variations in mineral components. The harzburgites contain the highest MgO (32–39 wt.%), FeO_T (10.4–13.5 wt.%) and the lowest Al_2O_3 (2.24–6.67 wt.%), CaO (1.17–3.8 wt.%), TiO_2 (0.09–0.4 wt.%) and alkali contents ($K_2O + Na_2O = 0.7$ to 1.5 wt.%) (Table 4, Fig. 5). The lherzolites have lower MgO (25.5–30.9 wt.%) contents and higher SiO_2 (45–47 wt.%), Al_2O_3 (5.8–8.7 wt.%), and CaO contents (3.2–4.5 wt.%) than the harzburgites (Table 4 and Fig. 5). For the olivine gabbro-norites, as MgO and FeO_T contents decrease (to 21.4–25.1 wt.% and 9.7–10.1 wt.%), SiO_2 (47.4–47.9 wt.%), Al_2O_3 (7.2–10.3 wt.%), CaO (5.4–7.6 wt.%), ($K_2O + Na_2O$) (1.3 to 2.2 wt.%) and TiO_2 contents (0.3–0.7 wt.%) increase (Fig. 5). The gabbro dykes plot on the same trends as the ultramafic rocks and are characterized by the higher SiO_2 (50.6–55.5 wt.%), Al_2O_3 (14–21.2 wt.%), ($K_2O + Na_2O$)
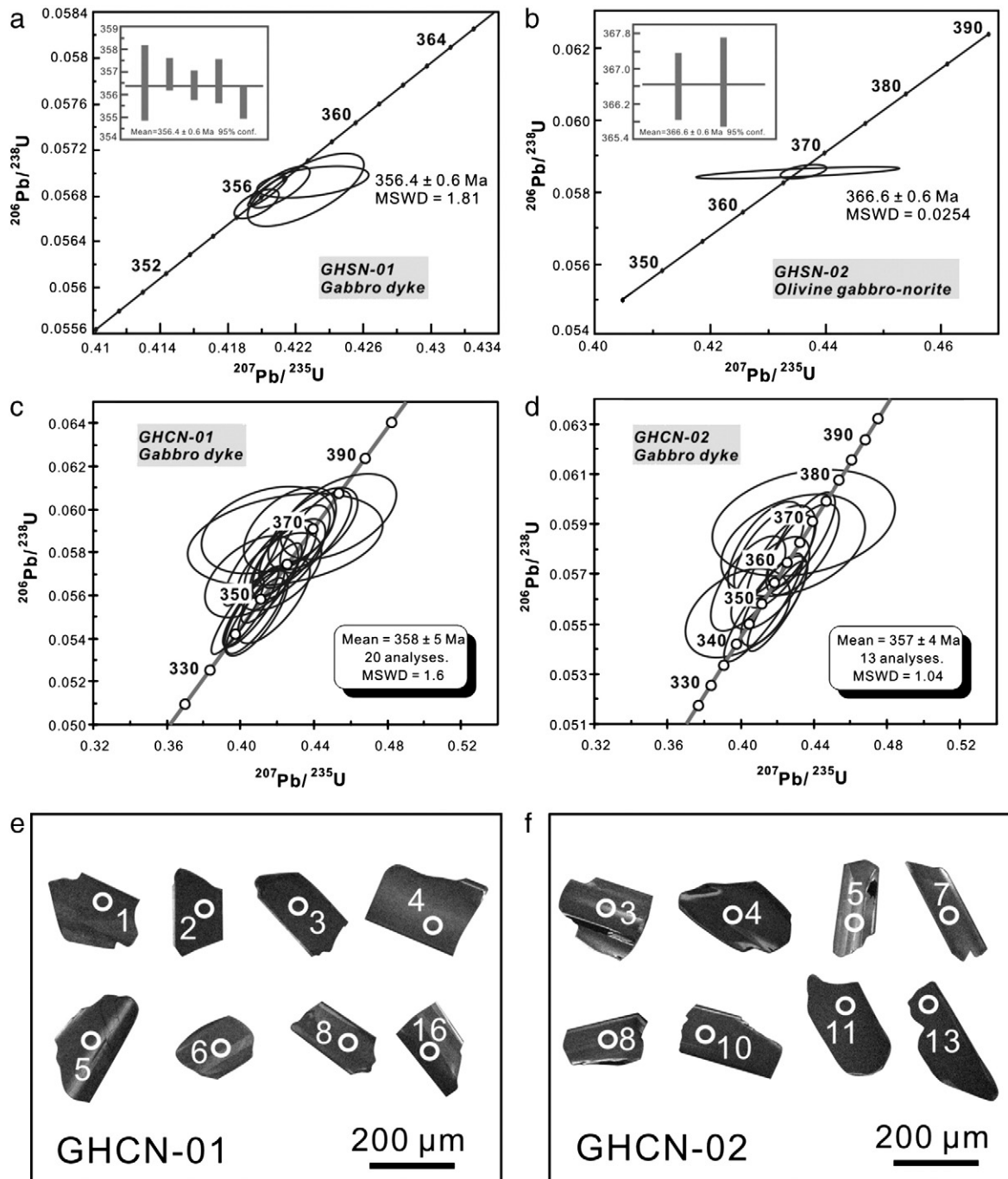
Fig. 4. (a and b) Concordia plots of ID-TIMS zircon U–Pb dating results for the Heishan gabbro dyke (GHSN-01) and the olivine gabbro-norite (GHSN-02); (c and d) concordia plots of SHRIMP zircon U–Pb analyses of the zircon separates from the Heishan gabbro dyke (GHCN-01 and GHCN-02); (e and f) cathodoluminescence (CL) images of representative zircons from the Heishan gabbro dyke (GHCN-01 and GHCN-02).

(3.5 to 4.7 wt.%) and CaO (5.7–11.0 wt.%), and the lowest MgO (6.9–15.3 wt.%), and FeO$_T$ (3.7–8.9 wt.%) contents (Fig. 5). These chemical variations are consistent with the petrographically observed order of crystallization Ol → Opx → Cpx → Pl, as described above.

On the trace element spider diagrams normalized to normal mid-ocean ridge basalts (N-MORB), the Heishan intrusive rocks are marked by strong enrichment in large ion lithophile elements (LILE) relative to heavy rare earth elements (HREE), similar to those of the Kalatongke and Pobei intrusions (Fig. 6) (Song and Li, 2009; Song et al., 2011; Xie et al., 2011). All samples show well developed negative Nb (Ta) anomalies and distinct positive K and Pb anomalies, which are common in arc volcanic rocks and clearly distinct from ocean

island basalts (OIB) and E-MORB (Fig. 6) (Sun and McDonough, 1989).

5.4. Sr, Nd and Pb isotopes

Although some of the Heishan samples have relatively high LOI, positive correlations do not exist between the concentrations of mobile trace elements (e.g., Rb, Sr, Pb) and their LOI (Table 4, Fig. 7). Particularly, Rb–Sr ratios are relatively constant when they are less than 0.35 (Fig. 7a). These plots indicate that the trace element compositions and Sr–Nd–Pb isotopic ratios of the Heishan rocks have been at most, only weakly affected by hydrothermal alteration.

Table 1b
SHRIMP U–Pb isotopic data for zircons of the samples from the Heishan intrusion.

| Sample/spot | ^{206}Pb[a] | ^{206}Pb[b] | U | Th | $^{232}Th/^{238}U$ | $^{207}Pb/^{206}Pb$ | ±1σ | $^{207}Pb/^{235}U$ | ±1σ | $^{206}Pb/^{238}U$ | ±1σ | Apparent ages (Ma) | | | | | |
	(ppm)	(%)	(ppm)	(ppm)			(%)		(%)		(%)	$^{206}Pb/^{238}U$	±1σ	$^{207}Pb/^{206}Pb$	±1σ	$^{208}Pb/^{232}Th$	±1σ
GHCN-01 gabbro dyke																	
GHCN-01-1	64.0	0.07	1343	1856	1.43	0.0533	1.1	0.41	2.3	0.0554	2.1	347.6	7.0	340	24	326	7
GHCN-01-2	51.4	0.09	1087	1429	1.36	0.0538	1.3	0.41	2.5	0.0550	2.1	345.3	7.0	364	30	324	7
GHCN-01-3	88.9	0.16	1862	3177	1.76	0.0533	1.5	0.41	2.7	0.0555	2.2	348.1	7.5	341	34	320	7
GHCN-01-4	35.6	0.16	711	622	0.90	0.0534	2.2	0.43	3.0	0.0583	2.1	365.1	7.6	346	49	349	10
GHCN-01-5	50.5	0.38	1066	1448	1.40	0.0541	1.9	0.41	2.8	0.0549	2.1	344.8	7.0	374	43	324	7
GHCN-01-6	32.7	0.22	661	597	0.93	0.0513	1.5	0.41	2.6	0.0574	2.1	359.7	7.4	256	35	340	8
GHCN-01-7	37.6	0.22	759	719	0.98	0.0530	2.0	0.42	2.9	0.0576	2.1	361.3	7.5	331	46	341	8
GHCN-01-8	36.2	0.13	713	748	1.08	0.0543	2.0	0.44	2.9	0.0589	2.1	369.1	7.6	383	45	352	9
GHCN-01-9	23.4	0.83	457	357	0.81	0.0509	5.4	0.41	5.8	0.0590	2.2	369.8	7.8	237	124	338	13
GHCN-01-10	57.4	0.24	1160	1167	1.04	0.0530	1.7	0.42	2.7	0.0575	2.1	360.2	7.4	329	38	343	8
GHCN-01-11	20.8	0.19	435	346	0.82	0.0545	2.1	0.42	3.1	0.0557	2.3	349.3	7.8	391	47	339	10
GHCN-01-12	43.4	0.00	916	1632	1.84	0.0524	1.2	0.40	2.4	0.0551	2.1	347.7	7.0	305	28	318	8
GHCN-01-13	27.8	0.67	565	539	0.98	0.0518	3.7	0.41	4.2	0.0569	2.1	356.6	7.4	279	84	336	11
GHCN-01-14	9.4	2.21	182	139	0.79	0.0524	7.8	0.42	8.1	0.0586	2.4	367.4	8.7	304	177	361	18
GHCN-01-15	25.7	0.38	505	415	0.85	0.0525	3.3	0.43	3.9	0.0590	2.2	369.8	7.8	306	75	356	10
GHCN-01-16	35.3	0.51	716	704	1.02	0.0536	2.8	0.42	3.5	0.0571	2.1	357.8	7.4	352	63	338	9
GHCN-01-17	31.8	0.31	639	573	0.93	0.0536	2.2	0.43	3.1	0.0577	2.1	361.8	7.5	353	51	345	9
GHCN-01-18	39.0	0.18	801	789	1.02	0.0535	1.6	0.42	2.7	0.0566	2.1	354.8	7.4	350	36	336	8
GHCN-01-19	20.0	0.51	387	340	0.91	0.0551	3.8	0.45	4.4	0.0597	2.2	373.6	8.1	417	86	362	11
GHCN-01-20	25.5	0.31	500	414	0.86	0.0540	2.8	0.44	3.5	0.0591	2.2	369.9	7.8	369	62	355	10
GHCN-02 gabbro dyke																	
GHCN-02-1	39.6	0.08	825	834	1.04	0.0541	1.8	0.42	2.8	0.0559	2.1	350.5	7.2	375	40	333	8
GHCN-02-2	66.8	0.00	1408	1638	1.20	0.0533	1.2	0.41	2.4	0.0552	2.1	346.3	7.0	343	26	330	8
GHCN-02-3	22.1	0.71	439	402	0.94	0.0536	5.7	0.43	6.2	0.0581	2.3	364.1	8.0	353	130	345	13
GHCN-02-4	40.2	0.37	823	935	1.17	0.0517	2.3	0.40	3.2	0.0566	2.2	355.1	7.7	274	53	328	9
GHCN-02-5	13.3	0.82	261	164	0.65	0.0533	7.0	0.43	7.4	0.0590	2.3	369.7	8.4	343	159	362	24
GHCN-02-6	41.5	0.16	826	836	1.05	0.0538	1.8	0.43	2.8	0.0584	2.1	365.7	7.6	364	42	353	8
GHCN-02-7	36.1	0.71	754	1128	1.55	0.0522	4.2	0.40	4.7	0.0554	2.1	347.7	7.2	294	97	324	8
GHCN-02-8	34.5	0.25	691	663	0.99	0.0517	2.5	0.41	3.3	0.0580	2.1	363.3	7.6	274	56	351	9
GHCN-02-9	27.3	0.39	546	598	1.13	0.0525	2.8	0.42	3.6	0.0579	2.2	362.6	7.7	306	64	346	12
GHCN-02-10	62.0	0.02	1296	2139	1.71	0.0547	1.3	0.42	2.5	0.0557	2.1	349.3	7.1	399	30	335	8
GHCN-02-11	53.7	0.14	1102	1199	1.12	0.0533	2.7	0.42	3.4	0.0566	2.1	355.2	7.3	343	61	333	8
GHCN-02-12	40.8	0.10	818	1048	1.32	0.0543	2.1	0.43	3.0	0.0580	2.1	363.5	7.6	385	47	343	8
GHCN-02-13	56.5	0.15	1144	1273	1.15	0.0533	1.9	0.42	2.8	0.0574	2.1	360.1	7.4	341	43	337	8

[a] Indicates the radiogenic Pb content.
[b] Indicates the common Pb content.

We selected the samples with low Rb–Sr (<0.35) for isotope analysis. Strontium, Nd and Pb isotope data for the Heishan intrusion are calculated to an initial age of 357 Ma (Table 5). All rocks have large ranges of initial $(^{87}Sr/^{86}Sr)_t$ ratios (0.7041 to 0.7087) and relatively restricted initial $(^{143}Nd/^{144}Nd)_t$ (0.5122 to 0.5124), with positive $\varepsilon_{Nd(t)}$ (+0.34 to +3.95) (Table 5, Fig. 8). There is no correlation between $(^{87}Sr/^{86}Sr)_t$ and LOI and two olivine gabbro-norite and two lherzolite samples have much higher $(^{87}Sr/^{86}Sr)_t$ than other samples. It suggests that the high $(^{87}Sr/^{86}Sr)_t$ values are not attributable to

hydrothermal alteration (Fig. 7b). In contrast, the Heishan country rocks, including siliceous slate and barite-containing slate, have much lower $\varepsilon_{Nd(t)}$ values (−7.6 to +2.1) and relatively higher initial $(^{87}Sr/^{86}Sr)_t$ ratios (0.7048 to 0.7103) than the intrusive rocks (Fig. 8).

The Heishan intrusive rocks have restricted $(^{206}Pb/^{204}Pb)_t$ (17.75–18.16), $(^{207}Pb/^{204}Pb)_t$ (15.55–15.64) and $(^{208}Pb/^{204}Pb)_t$ (37.71–38.29) values (Table 5). Fig. 9 illustrates that the Heishan intrusive rocks plot above the northern hemisphere reference line and between the enriched mantle end-members (EMI and EMII). The Heishan

Table 2
Representative olivine compositions from the Heishan sulfide-free ultramafic rocks of ZK1603.

Rock	Lherzolite	Harzburgite	Harzburgite	Harzburgite	Harzburgite	Harzburgite	Lherzolite
Sample	GHH-87	GHH-101	GHH-97	GHH-94	GHH-89	GHH-111	GHH-109
Depth/m	126	199	323	410	480	600	669
wt.%							
SiO₂	39.3–40.9	40.2–41.3	40.0–40.8	39.7–41.1	39.9–40.8	39.8–40.9	39.0–40.6
TiO₂	0–0.042	0.003–0.034	0.011–0.073	0–0.026	0–0.054	0.003–0.044	0–0.028
Al₂O₃	0–0.017	0–0.022	0–0.006	0–0.015	0–0.012	0–0.024	0–0.021
Cr₂O₃	0–0.072	0–0.066	0.001–0.033	0–0.049	0–0.026	0–0.114	0.003–0.088
FeO	14.4–16.2	13.3–14.1	13.5–14.6	12.1–13.2	14.6–17.0	12.8–14.2	14.6–17.7
MnO	0.172–0.241	0.162–0.215	0.181–0.212	0.161–0.211	0.186–0.267	0.131–0.229	0.186–0.274
MgO	42.3–43.9	43.5–45.0	44.1–45.2	45.6–46.1	42.6–44.5	43.6–45.4	41.4–44.1
NiO	0.136–0.228	0.19–0.273	0.243–0.335	0.24–0.318	0.283–0.428	0.246–0.404	0.185–0.299
CaO	0.103–0.209	0.069–0.142	0.087–0.147	0.088–0.157	0.066–0.139	0.059–0.154	0.132–0.192
Na₂O	0–0.03	0–0.038	0–0.041	0–0.038	0	0–0.008	0–0.045
Total	98.4–99.9	98.4–100.5	98.3–100.1	99.1–101	100–101	98.5–100.1	97.8–100.3
Fo	82.3–84.2	84.4–85.4	84.1–85.4	86.0–86.9	81.2–84.2	84.5–86.1	80.5–84.0

Table 3
Clinopyroxene compositions from the Heishan sulfide-free rocks of ZK1603.

Rock	Olivine gabbro-norite				Harzburgite	Harzburgite			Harzburgite		Harzburgite					Lherzolite
Sample	GHH-84				GHH-101	GHH-97			GHH-89		GHH-111					GHH-109
Depth/m	105				199	323			480		600					669
Spot	PY-1	PY-2	PY-3	PY-3	PY-2	PY-1	PY-2	PY-5	PY-2	PY-4	PY-1	PY-2	PY-6	PY-7	PY-8	PY-1
wt.%																
SiO_2	52.3	52.9	53.0	52.4	51.8	52.3	52.8	51.9	51.7	52.0	52.1	52.5	51.5	51.9	51.4	52.5
TiO_2	0.424	0.318	0.286	0.322	0.325	0.438	0.539	0.378	0.421	0.435	0.441	0.486	0.38	0.408	0.342	0.401
Al_2O_3	2.93	2.60	2.47	2.99	2.77	3.47	2.67	3.14	2.78	2.92	3.46	3.17	2.77	2.74	2.83	2.95
Cr_2O_3	0.646	0.85	0.892	0.929	0.865	1.16	0.943	1.04	0.981	0.985	1.02	0.798	1.01	0.959	0.887	0.793
FeO	4.98	4.47	4.65	5.08	4.25	4.47	4.07	4.41	4.56	4.61	4.27	4.45	4.25	4.23	4.41	5.07
MnO	0.129	0.115	0.134	0.139	0.119	0.111	0.121	0.108	0.115	0.112	0.119	0.145	0.125	0.146	0.115	0.125
MgO	16.5	17.5	17.8	17.4	17.0	17.3	15.8	16.7	17.2	17.1	16.2	16.8	17.3	17.3	17.7	17.3
CaO	20.5	20.7	20.0	19.6	20.7	20.4	22.3	20.7	20.5	20.8	20.4	21.1	20.6	20.6	20.5	20.4
Na_2O	0.247	0.257	0.253	0.277	0.183	0.313	0.422	0.243	0.25	0.328	0.322	0.286	0.251	0.258	0.287	0.323
K_2O	0	0	0	0	0	0	0	0	0	0	0	0	0	0	0	0
NiO	0.023	0.009	0.014	0.03	0.02	0.025	0.033	0.029	0.024	0.025	0.021	0.058	0.055	0.032	0.037	0.071
Total	98.7	99.7	99.4	99.2	98.0	100.1	99.7	98.7	98.5	99.3	98.4	99.8	98.3	98.6	98.6	99.9
Oxygen	6	6	6	6	6	6	6	6	6	6	6	6	6	6	6	6
Si	1.93	1.93	1.94	1.93	1.93	1.91	1.94	1.92	1.92	1.91	1.93	1.92	1.92	1.92	1.91	1.92
Al(iv)	0.066	0.067	0.061	0.074	0.073	0.093	0.064	0.081	0.083	0.086	0.073	0.080	0.085	0.080	0.094	0.079
Al(vi)	0.062	0.045	0.046	0.056	0.049	0.055	0.052	0.056	0.038	0.040	0.078	0.056	0.036	0.040	0.030	0.048
Ti	0.012	0.009	0.008	0.009	0.009	0.012	0.015	0.011	0.012	0.012	0.012	0.013	0.011	0.011	0.010	0.011
Cr	0.019	0.025	0.026	0.027	0.025	0.034	0.027	0.030	0.029	0.029	0.030	0.023	0.030	0.028	0.026	0.023
Fe^{3+}	0	0	0	0	0	0.004	0	0	0.016	0.025	0	0	0.024	0.012	0.060	0.013
Fe^{2+}	0.154	0.137	0.142	0.156	0.132	0.132	0.125	0.137	0.125	0.117	0.133	0.136	0.108	0.119	0.076	0.142
Mn	0.004	0.004	0.004	0.004	0.004	0.003	0.004	0.003	0.004	0.003	0.004	0.004	0.004	0.005	0.004	0.004
Mg	0.911	0.951	0.969	0.951	0.941	0.941	0.866	0.923	0.948	0.940	0.893	0.918	0.956	0.955	0.979	0.943
Ca	0.811	0.812	0.783	0.773	0.824	0.798	0.875	0.819	0.815	0.818	0.810	0.826	0.821	0.816	0.815	0.798
Na	0.018	0.018	0.018	0.020	0.013	0.022	0.030	0.017	0.018	0.023	0.023	0.020	0.018	0.019	0.021	0.023
K	0	0	0	0	0	0	0	0	0	0	0	0	0	0	0	0
Total	4.0	4.0	4.0	4.0	4.0	4.0	4.0	4.0	4.0	4.0	4.0	4.0	4.0	4.0	4.0	4.0
Wo	43.2	42.7	41.3	41.1	43.4	42.6	46.9	43.6	42.8	43.1	44.2	43.9	43.0	42.9	42.2	42.1
En	48.6	50.1	51.2	50.6	49.6	50.2	46.4	49.1	49.8	49.5	48.7	48.8	50.1	50.2	50.7	49.7
Fs	8.20	7.20	7.51	8.29	6.97	7.26	6.69	7.27	7.42	7.46	7.19	7.25	6.92	6.87	7.08	8.18

country rocks are marked by different Pb isotopes from the intrusive rocks (Fig. 9).

6. Discussion

6.1. Magma fractionation and parental magma compositions

The progressive upwards decrease of olivine contents from harzburgite through lherzolite to olivine gabbro-norite and the rock textures described above indicate that the fractionation is dominated by the crystallization and accumulation of olivine. Although the MgO contents of the harzburgites are much higher than those of the lherzolites (Fig. 10a), olivine in these rocks has accordant forsterite content (87 to 80%, Table 2). The very high proportion of ultramafic rocks (>90%) and the small variation in olivine composition indicate that the Heishan intrusion is a chamber in a magma plumbing system. The increase of SiO_2, Na_2O, K_2O and TiO_2 and incompatible elements towards the olivine gabbro-norite (Figs. 5 and 6) indicate a fractionation trend. The gabbro dykes plot on the same trends as the other rocks of the intrusion, indicating that they were comagmatic, although there are sharp contacts between them.

The forsterite percentages of the olivine (80–87) of the Heishan harzburgite and lherzolite suggest a mafic parental magma. These rocks define a trend towards olivine in the Al_2O_3 vs. MgO diagram (Fig. 10a), again indicating that olivine is the dominant cumulate phase. This permits us to use the method proposed by Chai and Naldrett (1992) to calculate the parental magma composition. We assume the olivine with the highest forsterite content (86.9%, Table 2) represents the earliest crystallized olivine from this parental magma and ~90% of iron is FeO in the Heishan rocks. On this basis, the MgO/(MgO + FeO) value of the parental magma is 0.668 according to the well established $K_D = (FeO/MgO)^{Ol}/(FeO/MgO)^L = 0.3$ (Roeder and

Emslie, 1970). The average contents of FeO_T and MgO in the harzburgites are 11.5 and 35.7 wt.%, respectively (Fig. 10b). The intersection point between the regression line at MgO/(MgO + FeO) = 0.668 and the trend from the olivine with the highest fosterite percentage (86.9%) to the average composition of the harzburgite indicates that the parental magma has 10.0 wt.% FeO_T and 11.3 wt.% MgO (Fig. 10b). This suggests that the Heishan intrusion has a high-MgO basaltic parental magma. The contents of the other oxides and trace elements of the parental magma can be calculated by the correlations between them and MgO (Chai and Naldrett, 1992). The composition of the calculated parental magma is comparable with the chilled margin of the gabbro dyke (GHS-86) (Table 6).

6.2. Tectonic implication

Many mafic–ultramafic intrusions with ages of 270–290 Ma occur in the Beishan and adjacent areas (e.g., Ao et al., 2010; Han et al., 2004; Jiang et al., 2006; Li et al., 2006; Qin et al., 2011; Su et al., 2010a,b, 2011; Tang et al., 2009; Wu et al., 2005; Zhou et al., 2004), except for the Late Carboniferous Tulaergen and Xiadong intrusion (San et al., 2010; Su et al., 2012). These ages overlap with those of the Tarim Permian continental flood basalts (278–290 Ma: Carroll et al., 1995; Chen et al., 1997; Li et al., 2008; Yang et al., 2006) and the related Bachu layered intrusion (273.7 ± 1.5 Ma, Zhang et al., 2008). Thus, a Tarim LIP link for these Permian mafic–ultramafic intrusions in northern Xinjiang has been recently proposed (Pirajno et al., 2008; Qin et al., 2011; Su et al., 2011).

Our new zircon SHRIMP U–Pb ages (358 ± 5 and 357 ± 4 Ma, Fig. 4c, d) and ID-TIMS U–Pb ages (356.4 ± 0.6 and 366.6 ± 0.6 Ma, Fig. 4a, b) indicate that the Heishan intrusion formed in the Late Devonian and cannot be connected with the Permian Tarim mantle plume. Our unpublished data indicate that the Late Devonian volcanics in the

Table 4
Representative contents of major oxides and trace elements of the Heishan intrusion.

Location	ZK1403	ZK1203		ZK1603				ZK803		Lherzolite					Surface
Rock	Harzburgite	Gabbro dyke	Harzburgite	Olivine gabbro-norite	Gabbro dyke	Lherzolite	Harzburgite	Olivine gabbro-norite		Lherzolite					Gabbro dyke
Sample depth (m)	GHH-06	GHH-42	GHH-49	GHH-82	GHH-83	GHH-85	GHH-101	GHH-142	GHH-141	GHH-140	GHH-139	GHH-138	GHH-137	GHH-136	GHS-85
	588	5.5	175	85	96	108	199	240	270	298	313	319	352	385	
Major elements (wt.%)															
SiO_2	40.4	50.4	40.4	45.0	51.0	40.8	40.0	45.4	45.3	43.9	43.8	43.1	41.6	42.4	51.7
TiO_2	0.270	0.620	0.150	0.360	0.420	0.260	0.150	0.620	0.570	0.440	0.440	0.430	0.420	0.440	0.650
Al_2O_3	4.92	19.86	4.14	6.82	20.68	5.99	5.59	9.77	9.77	8.16	7.18	6.85	6.54	6.37	17.6
FeO_T	11.9	3.5	10.5	9.7	3.7	10.6	10.1	9.80	9.60	10.2	10.7	11.0	11.6	11.2	5.25
MnO	0.190	0.070	0.170	0.160	0.080	0.170	0.160	0.170	0.160	0.170	0.170	0.180	0.180	0.180	0.100
MgO	30.4	8.0	35.0	23.1	6.7	27.0	30.5	20.3	20.7	24.0	25.6	26.8	26.5	27.4	7.50
CaO	2.78	8.08	2.24	7.19	10.7	3.86	2.99	5.16	5.38	4.22	3.66	3.62	3.43	3.34	8.29
Na_2O	0.670	3.70	0.690	0.910	2.91	0.690	0.750	1.49	1.52	1.22	1.11	1.03	0.980	0.950	3.27
K2O	0.180	0.760	0.160	0.310	0.630	0.240	0.150	0.640	0.590	0.570	0.480	0.450	0.410	0.420	0.770
P_2O_5	0.032	0.072	0.028	0.043	0.052	0.036	0.033	0.080	0.069	0.060	0.074	0.062	0.053	0.067	0.078
LOI	6.04	4.45	3.38	3.45	2.27	7.09	6.63	3.76	3.64	4.18	4.12	4.67	4.95	4.93	2.33
Total	99.4	100.0	98.5	98.3	99.7	98.1	98.5	98.5	98.5	98.5	98.8	99.7	98.2	99.3	98.23
Trace elements (ppm)															
Sc	10.3	17.4	9.84	25.500	21.5	14.5	10.2	19.5	19.3	15.5	15.0	14.9	15.1	14.6	27.1
Cr	2030	671	3030	1690	489	2110	2370	1350	1390	1660	1770	1800	1560	1950	114
Co	130	23	140	108	25.7	116	127	93.3	92.7	112	121	117	141	132	29.5
Ni	2060	116	1730	1000	102	1060	1340	844	901	1230	1480	1330	2810	1530	91.3
Cu	790	14.8	109	446	41.4	163	198	92.1	124	183	255	191	970	462	33.12
Rb	5.85	39.9	6.14	9.75	22.2	8.06	6.34	24.2	23.7	22.7	19.6	17.8	15.9	17.2	31.5
Sr	56.9	264	52.7	75.2	276	70.1	76.6	131	132	107	94.6	78.9	75.2	77.6	229
Y	6.55	15.8	4.31	10.9	11.7	6.74	4.68	15.0	13.2	10.8	11.1	10.7	9.14	10.2	16.4
Zr	29.2	71.3	21.8	42.4	49.6	37.0	23.8	74.6	69.7	63.3	62.7	61.2	52.0	56.4	86.9
Nb	0.789	1.93	0.602	1.11	1.40	0.937	0.580	2.18	1.82	1.70	1.76	1.61	1.42	1.57	2.29
Ba	28.9	151	32.0	48.4	394	49.4	36.7	110	81.9	61.8	73.1	66.5	56.3	63.8	235
La	1.72	5.81	1.44	3.05	4.26	2.31	1.59	5.49	4.87	4.18	4.63	3.84	3.44	3.83	6.36
Ce	4.36	13.2	3.28	7.29	10.0	5.25	3.67	12.5	11.2	9.62	10.6	9.04	7.75	9.15	14.7
Pr	0.591	1.77	0.477	1.01	1.35	0.710	0.513	1.71	1.46	1.28	1.41	1.22	1.16	1.26	1.91
Nd	2.65	7.76	2.19	4.69	6.30	3.15	2.28	7.61	6.62	5.74	6.23	5.53	5.04	5.63	8.35
Sm	0.819	2.15	0.796	1.38	1.59	1.02	0.724	2.25	1.80	1.57	1.62	1.49	1.31	1.41	2.09
Eu	0.291	0.962	0.281	0.568	0.730	0.406	0.284	0.766	0.731	0.596	0.592	0.566	0.488	0.506	0.850
Gd	0.976	2.53	0.817	1.69	2.00	1.17	0.850	2.50	2.33	1.90	1.92	1.82	1.55	1.74	2.52
Tb	0.179	0.436	0.147	0.284	0.330	0.208	0.132	0.415	0.388	0.304	0.307	0.315	0.264	0.276	0.458
Dy	1.04	2.64	0.861	1.80	2.03	1.23	0.780	2.51	2.34	1.90	1.92	1.86	1.60	1.75	2.68
Ho	0.243	0.567	0.200	0.422	0.455	0.284	0.190	0.598	0.533	0.433	0.431	0.430	0.379	0.385	0.625
Er	0.685	1.68	0.507	1.14	1.31	0.742	0.551	1.65	1.46	1.21	1.24	1.22	1.07	1.13	1.69
Tm	0.104	0.239	0.099	0.152	0.195	0.120	0.081	0.238	0.217	0.163	0.180	0.174	0.150	0.145	0.23
Yb	0.642	1.52	0.468	1.08	1.20	0.826	0.481	1.53	1.34	1.14	1.09	1.09	0.99	1.05	1.5
Lu	0.096	0.209	0.084	0.152	0.176	0.125	0.083	0.252	0.206	0.149	0.190	0.172	0.154	0.144	0.239
Hf	0.731	1.76	0.686	1.18	1.31	1.10	0.629	1.76	1.75	1.60	1.46	1.41	1.34	1.33	1.95
Th	0.554	1.48	0.464	0.779	1.10	0.775	0.410	1.47	1.41	1.34	1.21	1.18	0.98	1.01	2.12
U	0.147	0.384	0.143	0.217	0.334	0.229	0.143	0.383	0.386	0.335	0.301	0.321	0.299	0.240	0.48
Pb	2.94	2.49	1.73	3.25	2.54	2.43	1.42	3.60	3.64	3.14	3.96	3.04	4.98	3.54	4.20

FeO_T means total FeO. Tantalum (Ta) is below detection limit. The complete data is placed in Appendix A.
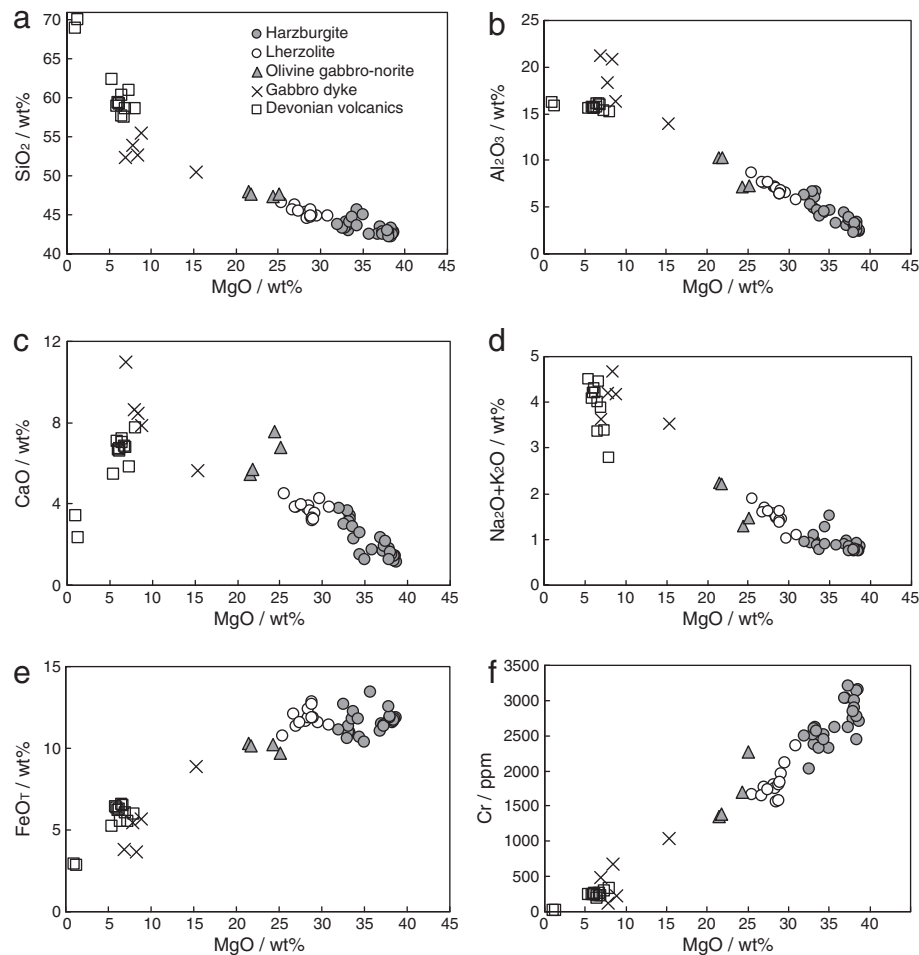
Fig. 5. Binary diagrams of oxides versus MgO for the Heishan rocks.
The fields of the Devonian volcanics (include andesites and rhyolites) in the Heishan area are after our unpublished data.

Heishan area show characteristics of typical arc volcanics, enriched in large ion lithophile elements, negative Nb (Ta) anomalies, and positive K and Pb anomalies (Fig. 6c). In the Th–Hf–Nb diagram, they plot in the field of island arc basalts (Fig. 11), also indicating a subduction environment. Whereas, the Tarim Permian basalts plot in the within-plate area (Fig. 11). The N-MORB normalized trace element patterns of the Heishan rocks are parallel to those of the Devonian volcanics (Fig. 6c), indicating that the Heishan intrusion probably formed from subduction-related magmatism. Consistently, the trace element compositions of the calculated Heishan parental magma and the Heishan olivine gabbro-norites and gabbro dykes are perfectly comparable with those of the Devonian volcanics (Fig. 6). In contrast, the Tarim mantle plume related Bachu gabbros and mafic–ultramafic dykes show OIB like trace element compositions (Fig. 6). In addition, the Heishan rocks have Sr–Nd–Pb isotope compositions similar to the Pacific active continental margin of the Americas and volcanics of island arc and active continental margins (Figs. 8 and 9).

Occurrences of the Paleozoic ophiolites along the Xingxingxia and Kawabulak faults and thick Devonian and Carboniferous calc-alkaline basaltic andesite–dacite–rhyolite and 378–328 Ma gabbro-diorite intrusions in the Beishan Fold Belt were thought to be evidence of S-dipping subduction of the South Tianshan ocean at least continuing to Devonian to Carboniferous (BGMRG, 1989; Charvet et al., 2007; Chen et al., 1999; Hu et al., 2000; Liu et al., 2011; Zhang and Guo, 2008). The geochemistry of the Devonian Heishan intrusion and volcanics provide new evidence to indicate that the Beishan Fold Belt at the northern Tarim was an active continental margin during Paleozoic. This also suggests S-dipping subduction of the South

Tianshan ocean beneath Beishan (Lin et al., 2009), although others have proposed N-dipping subduction (Allen et al., 1993; Chen et al., 1999; Qin et al., 2011; Windley et al., 1990; Xiao et al., 2004, 2008). An alternative interpretation is that the South Tianshan Ocean experienced two-way subduction during the Late Paleozoic (e.g., Song et al., 2011).

The Hongliuhe ophiolite crosscut by 405 ± 5 Ma granite (Zhang and Guo, 2008) suggests that the ocean basin represented by the Hongliuhe ophiolite closed before Late Devonian. Thus, the Heishan intrusion and associated Devonian volcanics in the area are not related to the closure of the ocean basin.

6.3. Mantle source

The mantle wedge is characterized by depletion in high field strength elements on account of the extraction of arc magmas, but enriched in LILE (such as Rb, Sr, Ba, Pb) and Th and U due to the addition of subducted materials (Johnson and Plank, 1999; Keppler, 1996; Pearce and Peate, 1995). On the other hand, the negative Nb (Ta) anomalies of the volcanics along arc zones and active continental margins have been argued to result from retained rutile during melting of subducted slab (e.g., Ayers and Watson, 1993; Stolz et al., 1996). The enrichment of Rb, Ba, Th, U, and Pb, low REE, and Nd depletion of the Heishan rocks relative to N-MORB suggest partial melting of the mantle wedge modified by subduction input (Fig. 6).
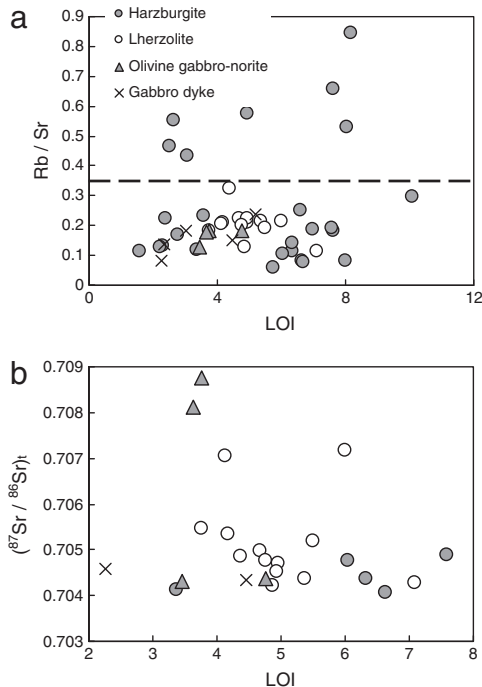
The mantle wedge may be low in both Sr and Nd isotopes (EMI) or low in ε_{Nd} and variable in $^{87}Sr/^{86}Sr$ (EMII) due to input of recycled lower crustal materials and subducted oceanic crust or continental
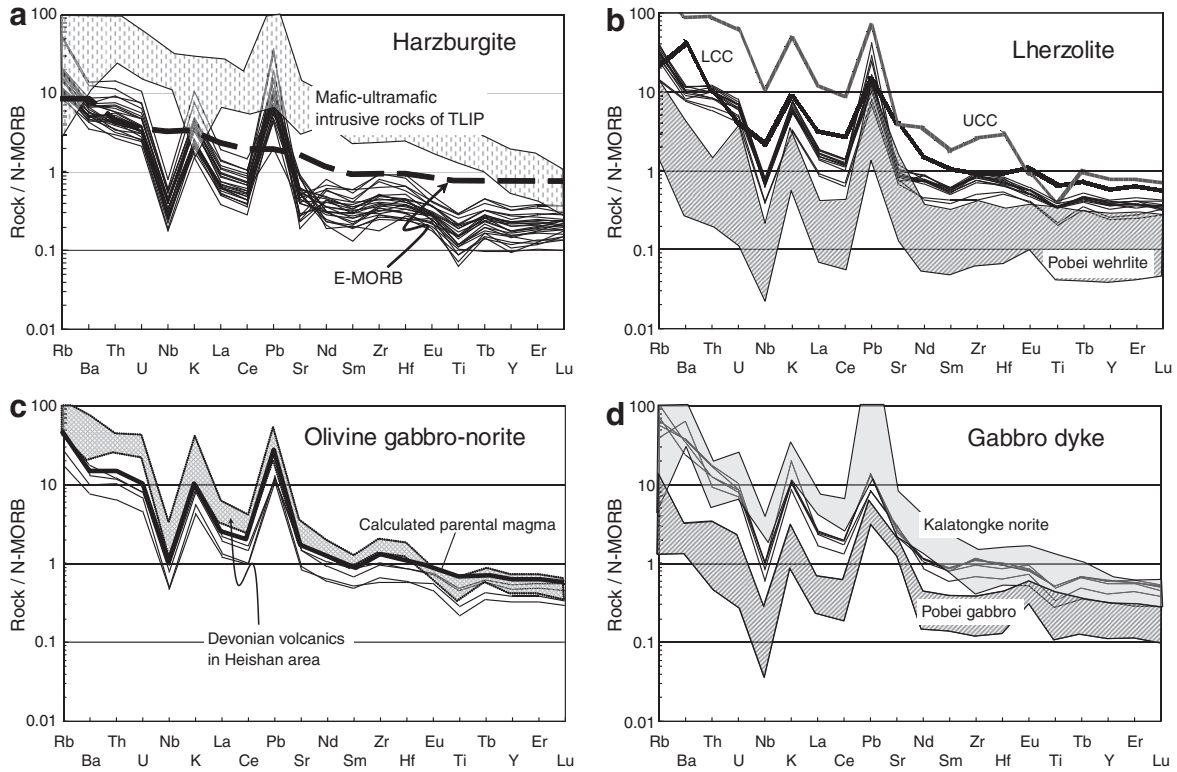
Fig. 6. N-MORB normalized trace element spider diagrams of the Heishan rocks.
N-MORB normalizing values from Sun and McDonough (1989). The data of E-MORB, UCC (upper continental crust) and LCC (lower continental crust) are from Sun and McDonough (1989) and Rudnick and Gao (2003) respectively. The fields of the Kalatongke and Pobei rocks are from Song and Li (2009), Xie et al. (2011), and Song et al. (2011), respectively. The data of mafic–ultramafic intrusive rocks of TLIP (the Tarim Large Igneous Province) are from Zhang et al. (2008) and Zhou et al. (2009). Devonian volcanics (include andesites and rhyolites) are from our unpublished data.

upper crust (Zindler and Hart, 1986). Thus, EMI and EMII have Sr–Nd isotope compositions similar to the lower and upper crusts, respectively. In the Sr–Nd isotope diagram (Fig. 8), the Heishan intrusive rocks plot within the area of the Permian Pobei mafic–ultramafic

Fig. 7. Plots of (a) Rb–Sr and (b) Sr isotope ratios vs. LOI for the Heishan rocks. The samples with Rb–Sr ratios lower than 0.35 are selected for Sr isotope analysis.

intrusion (e.g., Song et al., 2011; Xie et al., 2011), rather than the trendline to the wall rocks (siliceous slate and barite-containing slate) implying a minor contamination of wall rocks (Fig. 8). The low REE contents and enrichment of LILE of the Pobei intrusion were ascribed to decompression melting of the ascending asthenosphere and the adjacent overlying metasomatized subcontinental lithospheric mantle (Fig. 6) and the large variations of Sr–Nd isotopes were attributed to contamination by upper crust (Fig. 8) (e.g., Song et al., 2011). Correspondingly, the Heishan rocks have the relative high REE and LILE contents (Fig. 6), restricted $\varepsilon_{Nd(t)}$ values ($+3.95$ to $+0.34$), variable ($^{87}Sr/^{86}Sr)_t$ (0.7041 to 0.7087) (Fig. 8) and high ($^{207}Pb/^{204}Pb)_t$ and ($^{208}Pb/^{204}Pb)_t$ (Fig. 9). These similarities suggest that the primary magma of the Heishan intrusion was also derived from partial melting of the asthenosphere and metasomatized subcontinental lithospheric mantle modified by subducted materials. However, crustal contamination at deep level during ascending of the magmas cannot be ruled out (as discussed below), although it is very difficult to distinguish the Sr–Nd isotope signatures of the EMI and EMII reservoirs and inputs from lower and upper crusts in the Heishan rocks (Fig. 8). Clinopyroxene of the Heishan sulfide-free rocks fall in the overlay region of N-MORB and back-arc basin basalt, again suggesting that the primary magma of the Heishan intrusion has both MORB- and arc-like features, which was derived from partial melting of the asthenosphere and mantle wedge (Fig. 12) (e.g., Moghadam et al., 2010; Su et al., 2012; Xu et al., 2012).

6.4. Magma generation and evolution

The relatively low forsterite of olivine (80 to 87%, Table 2) in the Heishan harzburgites and lherzolites indicate that the high-Mg parental basaltic magmas had experienced some degree of fractional crystallization before they entered the intrusion. Thus, the primary magmas must

Table 5
Sr, Nd and Pb isotopes for the rocks of the Heishan intrusion and the surrounding rocks.

Rock	Gabbro dyke		Olivine gabbro-norite				Lherzolite								
Sample	GHH-42	GHH-83	GHH-82	GHH-84	GHH-141	GHH-142	GHH-85	GHH-87	GHH-108	GHH-109	GHH-135	GHH-136	GHH-137	GHH-138	GHH-139
Rb	39.9	22.2	9.75	15.2	23.7	24.2	8.06	7.72	18.4	17.1	13.6	17.2	15.9	17.8	19.6
Sr	264	276	75.2	83.8	132	131	70.1	60.4	84.9	80.0	67.0	77.6	75.2	78.9	94.6
Sm	2.15	1.59	1.38	1.28	1.80	2.25	1.02	1.11	1.44	1.36	1.41	1.41	1.31	1.49	1.62
Nd	7.76	6.30	4.69	4.34	6.62	7.61	3.15	3.29	5.30	5.28	5.48	5.63	5.04	5.53	6.23
Pb	2.49	2.54	3.25	3.86	3.64	3.60	2.43	2.06	4.21	4.98	8.73	3.54	4.98	3.04	3.96
Th	1.48	1.10	0.78	1.22	1.41	1.47	0.78	0.70	1.25	1.02	1.20	1.01	0.98	1.18	1.21
U	0.38	0.33	0.22	0.32	0.39	0.38	0.23	0.20	0.33	0.29	0.29	0.24	0.30	0.32	0.30
$^{87}Rb/^{86}Sr$	0.44	0.23	0.38	0.52	0.52	0.53	0.33	0.37	0.63	0.62	0.59	0.64	0.61	0.65	0.60
$^{87}Sr/^{86}Sr$	0.706559	0.705762	0.706202	0.707041	0.710743	0.711459	0.705968	0.706106	0.710352	0.707512	0.707759	0.707768	0.707804	0.708296	0.710079
$\pm2\sigma$	9	7	9	9	8	8	9	7	9	7	7	7	7	6	10
$(^{87}Sr/^{86}Sr)_t$	0.704341	0.704582	0.704299	0.704379	0.708107	0.708747	0.704281	0.704230	0.707170	0.704375	0.704780	0.704515	0.704701	0.704985	0.707037
$^{147}Sm/^{144}Nd$	0.17	0.15	0.18	0.18	0.16	0.18	0.20	0.20	0.16	0.16	0.16	0.15	0.16	0.16	0.16
$^{143}Nd/^{144}Nd$	0.512739	0.512737	0.512738	0.512724	0.512705	0.512706	0.512717	0.512733	0.512715	0.512696	0.512685	0.512678	0.512679	0.512668	0.512667
$\pm2\sigma$	3	2	4	8	3	4	7	7	5	2	3	6	2	4	3
$(^{143}Nd/^{144}Nd)_t$	0.512348	0.512381	0.512323	0.512308	0.512322	0.512289	0.512260	0.512257	0.512332	0.512333	0.512322	0.512325	0.512313	0.512288	0.512300
$\varepsilon Nd(t)$	3.31	3.95	2.81	2.52	2.79	2.15	1.59	1.53	2.99	3.00	2.80	2.85	2.61	2.13	2.37
$^{206}Pb/^{204}Pb$	18.30	18.47	18.35	18.45	18.41	18.49	18.49	18.41	18.28	18.25	18.19	18.30	18.29	18.43	18.44
$\pm2\sigma$	3	4	4	5	3	6	7	6	5	4	3	4	3	4	3
$^{207}Pb/^{204}Pb$	15.58	15.59	15.60	15.64	15.60	15.61	15.66	15.62	15.61	15.58	15.61	15.59	15.60	15.63	15.60
$\pm2\sigma$	1	2	2	2	1	3	3	3	2	1	1	2	1	2	1
$^{208}Pb/^{204}Pb$	38.40	38.39	38.36	38.63	38.53	38.59	38.66	38.56	38.26	38.27	38.32	38.38	38.40	38.64	38.54
$\pm2\sigma$	1	2	2	2	2	3	4	4	3	2	1	2	1	2	2
$(^{206}Pb/^{204}Pb)_t$	17.75	17.99	18.10	18.14	18.03	18.10	18.15	18.07	18.00	18.04	18.07	18.05	18.07	18.04	18.16
$(^{207}Pb/^{204}Pb)_t$	15.55	15.56	15.59	15.62	15.58	15.58	15.64	15.60	15.60	15.57	15.60	15.58	15.59	15.61	15.58
$(^{208}Pb/^{204}Pb)_t$	37.71	37.89	38.08	38.26	38.08	38.11	38.29	38.16	37.91	38.03	38.16	38.05	38.17	38.18	38.18

						Harzburgite					Metadacite	Metabasalt	Siliceous slate	Baritie-containing slate		
GHH-140	GHH-129	GHH-130	GHH-131	GHH-132	GHH-133	GHH-49	GHH-06	GHH-88	GHH-101	GHH-111	GHS-08	GHS-41	GHS-03	GHS-20	GHS-21	GHS-48
22.7	15.1	16.1	16.0	14.8	21.2	6.14	5.85	7.72	6.34	10.3	41.3	13.2	6.79	3.93	0.996	4.96
107	71.3	87.3	70.0	77.8	65.5	52.7	56.9	55.1	76.6	53.5	213	99.5	60.5	1080	582	816
1.57	1.40	1.52	1.44	1.60	1.64	0.796	0.819	1.08	0.724	0.875	4.9	1.39	0.604	1.18	1	0.999
5.74	4.58	6.40	5.50	5.30	6.24	2.19	2.65	3.49	2.28	3.58	24.9	4.82	3.01	4.88	3.96	4.17
3.14	12.08	7.31	7.10	12.38	4.29	1.73	2.94	2.77	1.42	9.53	7.37	2.38	3.24	3.69	2.14	2.87
1.34	1.28	1.44	1.29	1.20	1.40	0.46	0.55	0.69	0.41	0.77	6.68	0.93	0.86	0.87	0.54	0.76
0.34	0.32	0.38	0.34	0.34	0.36	0.14	0.15	0.19	0.14	0.22	1.47	0.25	3.05	1.40	0.95	0.97
0.61	0.61	0.53	0.66	0.55	0.94	0.34	0.30	0.41	0.24	0.56	0.56	0.38	0.32	0.01	0.00	0.02
0.708455	0.709301	0.708170	0.708704	0.707977	0.709601	0.705825	0.706275	0.706416	0.705284	0.707722	0.709380	0.706732	0.711971	0.708257	0.708312	0.708268
11	13	9	13	7	6	12	12	11	9	8	7	8	3	7	9	6
0.705341	0.706192	0.705463	0.705349	0.705185	0.704850	0.704115	0.704766	0.704360	0.704069	0.704896	0.706534	0.704785	0.710323	0.708204	0.708287	0.708179
0.17	0.18	0.14	0.16	0.18	0.16	0.22	0.19	0.19	0.19	0.15	0.12	0.17	0.12	0.15	0.15	0.14
0.512684	0.512728	0.512623	0.51266	0.512674	0.512692	0.512709	0.512694	0.512757	0.512709	0.512678	0.512444	0.512693	0.512172	0.512285	0.512146	0.512208
7	14	3	4	4	4	7	6	5	8	6	3	4	4	5	5	6
0.512298	0.512297	0.512288	0.512291	0.512248	0.512321	0.512197	0.512258	0.512321	0.512261	0.512333	0.512167	0.512286	0.511889	0.511944	0.511790	0.511870
2.33	2.30	2.13	2.18	1.35	2.78	0.34	1.55	2.77	1.61	3.01	−0.24	2.10	−5.66	−4.59	−7.60	−6.03
18.42	18.21	18.11	18.22	18.12	18.33	18.37	18.15	18.34	18.36	18.09	18.69	18.33	21.93	19.14	19.07	18.60
2	4	4	4	3	4	3	2	4	5	4	2	3	13	15	8	8
15.61	15.58	15.56	15.59	15.59	15.58	15.59	15.57	15.62	15.61	15.56	15.58	15.59	15.85	15.73	15.68	15.65
1	2	1	2	1	2	1	1	2	2	2	1	1	5	6	3	3
38.54	38.32	38.08	38.28	38.18	38.40	38.36	38.15	38.48	38.48	38.04	38.97	38.41	38.78	39.61	38.63	38.62
1	2	2	2	1	2	2	1	2	2	2	2	1	9	8	4	3
18.03	18.12	17.92	18.05	18.02	18.03	18.07	17.97	18.10	17.99	18.01	17.96	17.95	18.34	17.74	17.46	17.38
15.59	15.57	15.55	15.58	15.58	15.56	15.57	15.56	15.60	15.59	15.56	15.54	15.57	15.66	15.66	15.59	15.58
38.04	38.20	37.86	38.06	38.06	38.02	38.05	37.93	38.19	38.14	37.94	37.91	37.95	38.45	39.33	38.33	38.31
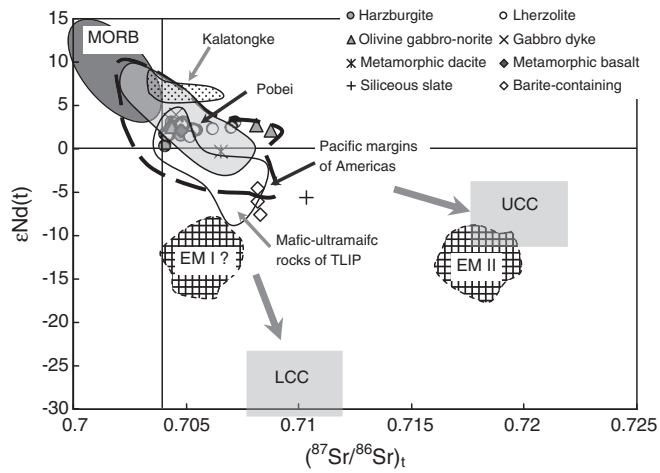
Fig. 8. Plot of $\varepsilon_{Nd(t)}$ versus $({}^{87}Sr/{}^{86}Sr)_t$ for the Heishan rocks. The $\varepsilon_{Nd(t)}$ and $({}^{87}Sr/{}^{86}Sr)_t$ values are normalized to 357 Ma.
The fields of EM I, EM II, UCC (upper continental crust) and LCC (lower continental crust) are after Zindler and Hart (1986) and Rudnick and Gao (2003), respectively. The field of the Kalatongke and Pobei intrusive rocks are after Zhang et al. (2006), Song and Li (2009), Xie et al. (2011) and Song et al. (2011), respectively. The data of mafic–ultramafic rocks of TLIP (the Tarim Large Igneous Province) are from Jiang et al. (2004), Zhang et al. (2008) and Zhou et al. (2009). The data of the Pacific margins of Americas (including the western California and the southern Chile–Argentina) are from Cole and Basu (1995), Miller et al. (2000), Stern and Kilian (1996), D'Orazio et al. (2001), and Gorring et al. (2003).
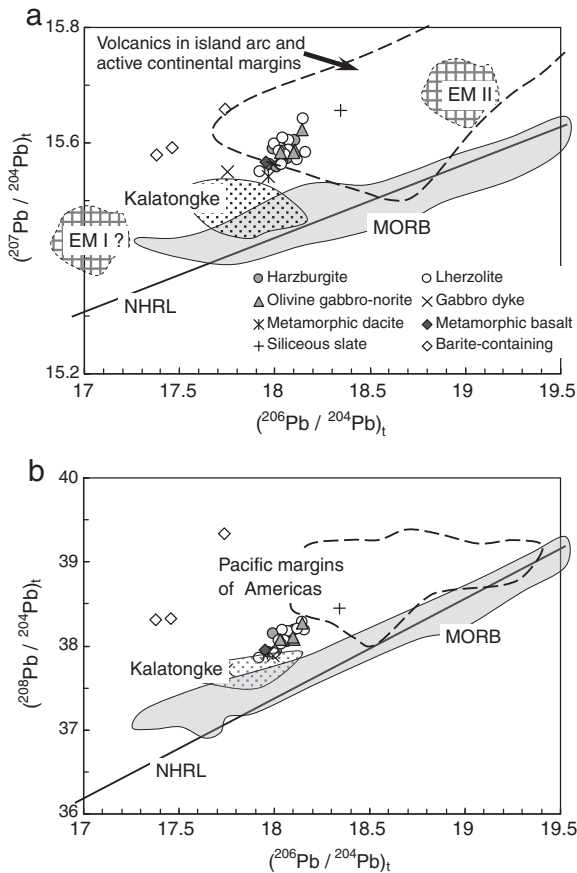
Fig. 9. Plots of (a) $({}^{207}Pb/{}^{204}Pb)_t$ and (b) $({}^{208}Pb/{}^{204}Pb)_t$ versus $({}^{206}Pb/{}^{204}Pb)_t$ for the Heishan rocks. The initial Pb isotope values are normalized to 357 Ma. NHRL is Northern Hemisphere Reference Line.
The fields of EM I and EM II are after Zindler and Hart (1986). The field of the rocks of the Kalatongke intrusion is after Song and Li (2009). The fields of volcanics of island and active continental margins and the Pacific margins of Americas (including the western California and the southern Chile–Argentina) are from Wilson (1989), Miller et al. (2000), Stern and Kilian (1996), D'Orazio et al. (2001), and Gorring et al. (2003).
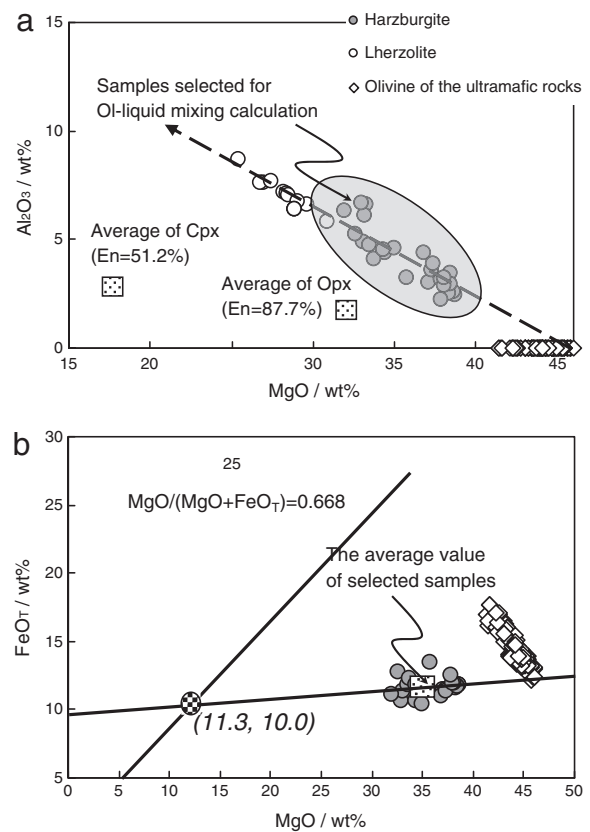
Fig. 10. (a) Plots of MgO vs. Al_2O_3 of the Heishan harzburgites and lherzolites. (b) Extrapolation of the variation diagram of FeO_T vs. MgO to estimate the parental magma composition of the Heishan intrusion. The parental magma has ~11.3 wt.% MgO and ~10 wt.% FeO_T.
The average compositions of Cpx (clinopyroxene, En = 51.2%) and Opx (orthopyroxene, En = 87.7%) of the harzburgites and lherzolites in (a) are from our unpublished data.

have had MgO contents higher than 11.3 wt.% and were produced by high degree partial melting. However, the calc-alkaline felsic and intermediate magmas derived from parental basalts generated in mantle wedge are the most common in arcs and active continental margins (e.g., Cole and Stewart, 2007; Crawford et al., 1987; Florisbal et al., 2009). Experiments have indicated that the solidus temperatures of peridotite or lherzolite containing H_2O are several hundred degrees lower than that of dry lherzolite. Thus, high-Mg basaltic or picritic magmas in the active continental margins may be produced by partial melting of metasomatized mantle T < 1300 °C when heated by upwelling asthenospheric mantle (e.g., Green and Falloon, 1998; Hirose and Kawamoto, 1995; Takazawa et al., 2000). Upwelling of asthenosphere in subduction and collision zones is generally due to roll-back of the subducting slab or slab break-off (e.g., Davies and von Blanckenburg, 1995; Kelemen et al., 2003; Martinez and Taylor, 2002; Thorkelson, 1996; Zimmer et al., 2010). Increasing post-collisional extension may lead to decompression melting of the convective asthenosphere, and the generation of tholeiitic magmas (e.g., Crawford and Berry, 1992). However, no evidence for a Devonian–Carboniferous back-arc spreading basin has been found in the Beishan Fold Belt, and closure of the South Tianshan ocean took place in Carboniferous–Permian (Laurent-Charvet et al., 2003; Wang et al., 2010; Xiao et al., 2004, 2008, 2010). Thus, the generation of high-Mg basaltic magma in the Heishan area should not be due to roll-back of the subducting slab or post-collisional extension.

Subducting slab break-off may occur due to slow subduction of a hot young oceanic slab or the cessation of subduction because of collision (Davies and von Blanckenburg, 1995; Thorkelson, 1996). The asthenosphere may rise rapidly into the lithosphere break and

Table 6
Chemical composition of calculated parental magma and analytical chilled margin, Heishan.

Major elements (wt.%)

	SiO$_2$	TiO$_2$	Al$_2$O$_3$	FeO$_T$	MnO	MgO	CaO	Na$_2$O	K2O	P$_2$O$_5$	LOI	Total
Calculated parental magma	50.8	0.914	14.2	10.0	0.167	11.8	7.56	1.90	0.901	0.112		99.9
The chilled marginal gabbro	49.6	0.910	13.5	8.0	0.15	12.1	6.79	3.06	0.570	0.089	3.07	98.82

Trace elements (ppm)

| Sc	Cr	Co	Ni	Cu	Rb	Sr	Y	Zr	Nb	Ba	La	Ce	Pr	Nd	Sm	Eu	Gd	Tb	Dy	Ho	Er	Tm	Yb	Lu	Hf	Th	U	Pb
23.5	590		300		30.3	160	19.1	106	2.71	108	6.99	15.9	2.19	9.73	2.54	0.960	3.14	0.516	3.21	0.739	1.99	0.283	1.89	0.282	2.50	2.05	0.517	9.41
23.6		49.8	300	11.80	21	150	19.7	89.8	2.65	180	6.18	15.3	2.04	9.12	2.63	0.886	3.14	0.537	3.33	0.764	2.01	0.29	1.83	0.275	2.09	1.98	0.413	3.54

FeO$_T$ means total FeO.
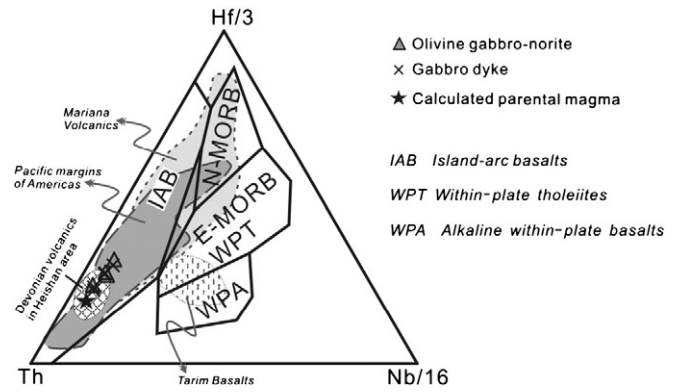
Fig. 11. Plots of the Heishan olivine gabbro-norites and gabbro dykes (SiO$_2$ > 47 wt.%) in Th–Hf–Nb discrimination diagram (Wood, 1980).
The data of Mariana volcanics (including Mariana arc, rift and back-arc basin) are from Pearce et al. (2005). The data of the Pacific margins of Americas (including the western California and the southern Chile–Argentina) are from Cole and Basu (1995), Stern and Kilian (1996), D'Orazio et al. (2001), and Gorring et al. (2003). The data of Tarim basalts are from Jiang et al. (2004) and Zhou et al. (2009). Devonian volcanics (including andesites and rhyolites) are from our unpublished data.

probably melt when it rises to depths shallower than 50 km if the slab break-off occurs at a very shallow depth. In the Pacific margins of the Americas (southern Chile–Argentina and western California), basalts are attributed to high degree decompression partial melting of asthenosphere upwelling to a depth less than 50 km on account of subduction slab break-off (e.g., Cole and Basu, 1995; D'Orazio et al., 2001; Gorring et al., 2003; Miller et al., 2000). More common slab break-off occurs at a depth larger than 50 km where decompression melting of the asthenosphere is difficult. In such a situation, upwelling of the hot asthenosphere leads to melting the metasomatized lithosphere which has a lowered solidus due to the presence of hydrated minerals, such as phlogopite and amphibole (Davies and von Blanckenburg, 1995; Green and Falloon, 1998; Takazawa et al., 2000). Enrichment of LILE and moderate ε$_{Nd(t)}$ values suggest that the Heishan intrusion is most likely associated with partial melting of the metasomatized mantle wedge heated by upwelling asthenosphere due to slab break-off.

Involvement of crustal sulfur is very important for the mantle derived magma to reach sulfide segregation, because sulfide solubility of basaltic magma increases as pressure decreases (e.g., Barnes and Lightfoot, 2005; Keays and Lightfoot, 2007, 2010; Naldrett, 1999; Ripley et al., 2003). The presence of the economic Ni–Cu sulfide ore bodies in the Heishan intrusion also indicates significant crustal contamination. However, in the Sr–Nd and Pb isotope diagrams, the country rocks plot on trends different from those of the Heishan
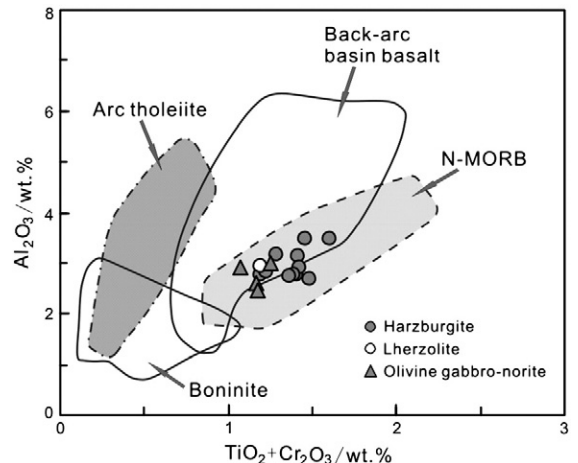
Fig. 12. Al$_2$O$_3$ vs. TiO$_2$ + Cr$_2$O$_3$ diagram for clinopyroxene from the Heishan rocks. After Moghadam et al. (2010) and references therein.

intrusive rocks (Figs. 8 and 9), implying that the country rocks are not the dominant contaminant. We propose that the magmas had experienced crustal assimilation at deep levels, before they entered the Heishan intrusion, although it is difficult to estimate the intensity of the crustal contamination.

7. Conclusions

The Heishan intrusion was formed in the active continental margin of the Tarim craton during Late Devonian ($\sim357 \pm 4$ Ma). Its parental magma is a high-Mg basaltic magma with ~11.3 wt.% MgO and ~10.0 wt.% FeO$_T$. The high-Mg primary magmas were derived from partial melting of the asthenosphere and metasomatized subcontinental lithospheric mantle modified by subducted materials, triggered by upwelling of asthenosphere due to break-off of subduction slab. The magmas had experienced fractionation–assimilation processes before they entered the Heishan intrusion.

Appendix A

Table 4
Contents of major oxides and trace elements of the Heishan intrusion.

Location	ZK1403									ZK1203							ZK1603
Rock	Harzburgite									Gabbro dyke	Harzburgite						Olivine gabbro-norite
Sample	GHH-40	GHH-34	GHH-30	GHH-27	GHH-24	GHH-20	GHH-10	GHH-06	GHH-02	GHH-42	GHH-44	GHH-49	GHH-50	GHH-63	GHH-68	GHH-71	GHH-82
Depth (m)	47	136	229	283	334	418.5	509	588	635	5.5	15	175	278	402.5	598.5	677	85
Major elements (wt.%)																	
SiO_2	42.0	41.4	41.0	40.9	41.7	38.9	38.6	40.4	37.6	50.4	39.9	40.4	41.3	41.0	40.2	40.3	45.0
TiO_2	0.370	0.190	0.190	0.180	0.200	0.090	0.110	0.270	0.140	0.620	0.080	0.150	0.140	0.150	0.220	0.260	0.360
Al_2O_3	2.92	3.08	2.31	2.46	2.41	3.18	3.51	4.92	2.62	19.86	6.16	4.14	3.47	2.75	2.09	3.09	6.82
FeO_T	11.1	11.3	11.3	11.3	11.1	10.7	10.3	11.9	10.4	3.5	10.2	10.5	11.0	11.4	11.7	12.7	9.7
MnO	0.180	0.180	0.180	0.180	0.180	0.170	0.170	0.190	0.170	0.070	0.160	0.170	0.180	0.180	0.180	0.190	0.160
MgO	35.9	36.9	37.0	37.0	36.9	35.4	33.9	30.4	33.9	8.0	31.0	35.0	36.0	36.4	35.4	33.9	23.1
CaO	1.62	1.77	1.12	1.37	1.15	1.35	1.97	2.78	1.25	8.08	3.15	2.24	1.83	1.41	1.17	1.62	7.19
Na_2O	0.610	0.550	0.520	0.530	0.570	0.550	0.490	0.670	0.380	3.700	0.750	0.690	0.650	0.550	0.450	0.590	0.910
K2O	0.330	0.180	0.290	0.180	0.310	0.170	0.190	0.180	0.270	0.760	0.110	0.160	0.160	0.170	0.260	0.240	0.310
P_2O_5	0.044	0.030	0.038	0.032	0.037	0.028	0.026	0.032	0.040	0.072	0.022	0.028	0.031	0.038	0.032	0.038	0.043
LOI	3.06	2.29	2.62	2.39	2.5	6.36	7.62	6.04	10.1	4.45	5.76	3.38	2.20	2.76	4.94	3.59	3.45
Total	99.8	99.6	98.4	98.1	98.7	98.5	98.4	99.4	98.4	100.0	98.7	98.5	98.6	98.4	98.4	98.3	98.3
Trace elements (ppm)																	
Sc	12.4	8.98	8.00	8.89	8.57	5.87	7.68	10.3	5.84	17.4	8.97	9.84	9.02	8.94	8.89	10.6	25.500
Cr	3040	2730	2710	3150	3130	2780	2620	2030	2440	671	2610	3030	3200	3000	2850	2610	1690
Co	143	151	146	152	150	143	133	130	130	23	128	140	148	168	188	177	108
Ni	2190	2410	2000	2490	2280	2100	1780	2060	2270	116	1430	1730	2050	3000	4140	2990	1000
Cu	337	323	104	379	118	128	74	790	260	14.8	152	109	216	761	1490	1080	446
Rb	10.9	6.55	11.4	6.05	11.5	5.59	8.41	5.85	10.8	39.9	4.66	6.14	5.25	5.97	9.90	8.94	9.75
Sr	25.1	49.7	20.7	26.8	24.8	48.2	46.5	56.9	36.1	264	76.9	52.7	40.6	35.3	17.2	38.1	75.2
Y	9.25	5.03	5.62	4.96	5.63	3.07	3.35	6.55	4.24	15.8	2.62	4.31	4.08	4.31	6.02	6.25	10.9
Zr	47.0	25.7	36.4	26.3	36.9	25.7	19.5	29.2	21.1	71.3	13.3	21.8	23.4	27.1	30.3	38.1	42.4
Nb	1.34	0.698	1.02	0.818	1.02	0.607	0.523	0.789	0.698	1.93	0.413	0.602	0.628	0.628	0.953	0.944	1.11
Ba	45.7	36.6	43.6	33.3	41.6	33.0	29.8	28.9	38.6	151	27.5	32.0	32.3	27.9	35.3	31.4	48.4
La	2.77	1.56	2.39	1.65	2.24	1.58	1.30	1.72	1.89	5.81	0.971	1.44	1.59	1.75	1.85	2.16	3.05
Ce	6.59	3.93	5.50	4.06	5.08	3.28	2.98	4.36	4.25	13.2	2.11	3.28	3.64	3.97	4.60	5.03	7.29
Pr	0.939	0.534	0.740	0.564	0.660	0.421	0.398	0.591	0.534	1.77	0.318	0.477	0.492	0.549	0.658	0.706	1.01
Nd	4.54	2.60	3.18	2.67	2.99	1.71	1.81	2.65	2.21	7.76	1.40	2.19	2.10	2.29	3.18	3.01	4.69
Sm	1.56	0.667	0.772	0.853	1.01	0.561	0.497	0.819	0.621	2.15	0.539	0.796	0.686	0.576	0.943	0.878	1.38
Eu	0.439	0.225	0.247	0.286	0.304	0.191	0.179	0.291	0.230	0.962	0.240	0.281	0.251	0.291	0.298	0.324	0.568
Gd	1.60	0.832	0.946	0.947	1.04	0.572	0.522	0.976	0.720	2.53	0.512	0.817	0.791	0.861	1.043	1.000	1.69
Tb	0.301	0.154	0.170	0.161	0.191	0.112	0.094	0.179	0.110	0.436	0.097	0.147	0.132	0.118	0.164	0.173	0.284
Dy	1.74	0.876	0.986	0.890	1.11	0.548	0.604	1.04	0.674	2.64	0.523	0.861	0.779	0.775	1.00	1.08	1.80
Ho	0.398	0.200	0.224	0.227	0.237	0.121	0.138	0.243	0.143	0.567	0.132	0.200	0.187	0.172	0.223	0.249	0.422
Er	1.09	0.611	0.616	0.565	0.654	0.356	0.408	0.685	0.398	1.68	0.379	0.507	0.533	0.502	0.668	0.644	1.14
Tm	0.172	0.078	0.089	0.098	0.107	0.061	0.058	0.104	0.058	0.239	0.066	0.099	0.088	0.071	0.104	0.104	0.152
Yb	1.02	0.581	0.623	0.533	0.677	0.331	0.389	0.642	0.423	1.52	0.373	0.468	0.521	0.438	0.608	0.638	1.08
Lu	0.170	0.083	0.089	0.094	0.111	0.069	0.061	0.096	0.070	0.209	0.080	0.084	0.102	0.074	0.091	0.108	0.152
Hf	1.35	0.604	0.942	0.904	1.07	0.629	0.530	0.731	0.530	1.76	0.563	0.686	0.782	0.699	0.781	0.847	1.18
Th	0.902	0.475	0.839	0.623	0.831	0.491	0.415	0.554	0.492	1.48	0.321	0.464	0.595	0.514	0.580	0.670	0.779
U	0.266	0.182	0.240	0.169	0.225	0.153	0.117	0.147	0.154	0.384	0.100	0.143	0.170	0.130	0.155	0.174	0.217
Pb	2.82	3.23	1.31	2.15	1.92	1.80	1.32	2.94	0.592	2.49	1.62	1.73	2.19	2.61	4.61	4.23	3.25

Table 4 (continued)

Location																	ZK803
Rock	Gabbro dyke	Olivine gabbro-norite	Lherzolite		Harzburgite										Lherzolite		Gabbro dyke
Sample	GHH-83	GHH-84	GHH-85	GHH-87	GHH-101	GHH-99	GHH-98	GHH-97	GHH-95	GHH-94	GHH-88	GHH-116	GHH-113	GHH-111	GHH-109	GHH-108	GHH-144
Depth (m)	96	105	108	126	199	260	290	323	385	410	472	525	555	600	669	678	209
Major elements (wt.%)																	
SiO_2	51.0	44.6	40.8	42.0	40.0	39.2	41.5	40.8	40.6	41.4	41.1	41.3	39.6	39.7	41.8	42.1	47.5
TiO_2	0.420	0.280	0.260	0.280	0.150	0.110	0.330	0.370	0.190	0.360	0.270	0.240	0.280	0.240	0.420	0.450	0.660
Al_2O_3	20.68	6.84	5.99	5.44	5.59	6.04	3.95	4.53	5.87	4.21	4.39	3.76	3.17	4.08	6.63	7.02	13.11
FeO_T	3.7	9.1	10.6	10.7	10.1	9.6	9.7	10.5	10.3	9.5	11.0	11.3	11.4	10.7	11.0	11.2	8.3
MnO	0.080	0.150	0.170	0.180	0.160	0.160	0.150	0.170	0.160	0.150	0.180	0.190	0.160	0.160	0.180	0.170	0.150
MgO	6.7	23.5	27.0	28.9	30.5	29.8	31.3	30.6	29.6	32.1	31.3	31.2	31.8	31.2	26.4	24.7	14.3
CaO	10.69	6.32	3.86	3.62	2.99	3.33	1.36	2.89	3.52	1.14	2.66	2.11	1.56	2.32	3.61	3.55	5.32
Na_2O	2.91	0.960	0.690	0.790	0.750	0.720	0.610	0.690	0.700	0.640	0.570	0.450	0.450	0.530	0.910	0.950	1.87
K2O	0.630	0.400	0.240	0.230	0.150	0.130	0.540	0.330	0.180	0.760	0.240	0.270	0.350	0.290	0.450	0.530	1.440
P_2O_5	0.052	0.049	0.036	0.031	0.033	0.025	0.057	0.044	0.028	0.070	0.043	0.048	0.047	0.044	0.070	0.054	0.083
LOI	2.27	4.76	7.09	4.87	6.63	7.98	7.63	6.61	6.68	8.18	6.32	6.96	8.06	7.59	5.37	6.01	5.20
Total	99.7	98.2	98.1	98.6	98.5	98.5	98.6	99.1	99.3	100.0	99.6	99.5	98.5	98.5	98.3	98.3	99.1
Trace elements (ppm)																	
Sc	21.5	21.3	14.5	16.2	10.2	8.37	8.52	14.5	12.6	6.45	13.0	11.4	9.09	9.50	14.6	13.0	20.7
Cr	489	2270	2110	2360	2370	2520	2520	2600	2500	2320	2570	2330	2380	2450	1750	1640	1040
Co	25.7	102	116	121	127	121	125	130	132	128	137	144	180	157	124	130	72.1
Ni	102	989	1060	1130	1340	1430	1680	1810	2240	1500	2370	2940	4510	3270	1750	2700	593
Cu	41.4	274	163	145	198	95.1	186	286	612	101	467	858	2140	1500	487	1210	79.5
Rb	22.2	15.2	8.06	7.72	6.34	6.24	28.0	11.6	6.18	30.0	7.72	8.89	11.6	10.3	17.1	18.4	58.1
Sr	276	83.8	70.1	60.4	76.6	75.9	42.7	46.2	81.9	35.5	55.1	47.0	21.9	53.5	80.0	84.9	245
Y	11.7	9.03	6.74	7.23	4.68	3.55	7.97	9.99	4.84	9.14	7.03	6.38	7.72	6.55	10.30	11.71	16.6
Zr	49.6	49.1	37.0	31.4	23.8	18.7	59.8	68.5	28.5	70.4	32.6	34.1	55.8	37.3	62.8	63.3	80.9
Nb	1.40	1.12	0.937	0.889	0.580	0.659	1.44	1.30	0.599	1.90	0.915	0.914	1.24	1.08	1.46	1.47	2.28
Ba	394	62.2	49.4	47.7	36.7	33.1	78.1	54.5	41.2	87.3	45.7	48.2	45.9	45.2	59.6	62.8	214.0
La	4.26	3.34	2.31	2.13	1.59	1.34	3.52	3.39	1.54	4.78	2.38	2.42	2.99	2.75	3.81	3.61	6.12
Ce	10.0	7.52	5.25	4.80	3.67	2.89	7.83	7.91	3.32	11.0	5.49	5.58	7.03	6.33	8.76	8.48	14.20
Pr	1.35	0.975	0.710	0.718	0.513	0.408	0.995	1.08	0.496	1.36	0.749	0.768	0.956	0.882	1.26	1.15	1.98
Nd	6.30	4.34	3.15	3.29	2.28	1.69	4.38	4.89	2.29	5.83	3.49	3.34	4.17	3.58	5.28	5.30	8.58
Sm	1.59	1.28	1.02	1.11	0.724	0.511	1.09	1.55	0.776	1.41	1.08	0.961	1.20	0.875	1.36	1.44	2.35
Eu	0.730	0.465	0.406	0.420	0.284	0.261	0.364	0.513	0.303	0.422	0.375	0.312	0.382	0.378	0.538	0.505	0.883
Gd	2.00	1.42	1.17	1.22	0.850	0.697	1.50	1.69	0.898	1.55	1.26	1.15	1.36	1.11	1.78	1.78	2.85
Tb	0.330	0.233	0.208	0.231	0.132	0.102	0.217	0.302	0.176	0.263	0.215	0.190	0.221	0.186	0.295	0.305	0.461
Dy	2.03	1.55	1.23	1.31	0.780	0.626	1.33	1.89	0.906	1.60	1.27	1.04	1.31	1.19	1.78	1.86	2.86
Ho	0.455	0.351	0.284	0.312	0.190	0.121	0.300	0.443	0.220	0.347	0.300	0.253	0.316	0.259	0.420	0.440	0.641
Er	1.31	0.967	0.742	0.828	0.551	0.371	0.879	1.15	0.581	1.03	0.858	0.711	0.778	0.728	1.12	1.12	1.82
Tm	0.195	0.135	0.120	0.142	0.081	0.054	0.138	0.157	0.094	0.147	0.134	0.107	0.124	0.107	0.172	0.182	0.250
Yb	1.20	0.958	0.826	0.810	0.481	0.350	0.852	1.02	0.548	1.03	0.775	0.677	0.786	0.735	1.06	1.13	1.66
Lu	0.176	0.135	0.125	0.147	0.083	0.061	0.130	0.171	0.08	0.137	0.140	0.111	0.114	0.107	0.166	0.165	0.248
Hf	1.31	1.20	1.10	1.04	0.629	0.498	1.35	1.87	0.761	1.70	0.942	0.846	1.17	0.910	1.49	1.55	2.08
Th	1.10	1.22	0.775	0.701	0.410	0.385	1.34	1.06	0.484	1.73	0.688	0.703	1.11	0.773	1.02	1.25	1.50
U	0.334	0.323	0.229	0.196	0.143	0.122	0.343	0.358	0.160	0.498	0.185	0.225	0.301	0.221	0.292	0.329	0.411
Pb	2.54	3.86	2.43	2.06	1.42	2.63	4.32	2.88	3.02	2.07	2.77	3.43	11.1	9.53	4.98	4.21	4.14

	Olivine gabbro-norite		Lherzolite										Surface Gabbro dyke		
	GHH-142	GHH-141	GHH-140	GHH-139	GHH-138	GHH-137	GHH-136	GHH-135	GHH-133	GHH-132	GHH-130	GHH-129	GHS-84	GHS-85	GHS-86
	240	270	298	313	319	352	385	400	416	445	470	484			
	45.4	45.3	43.9	43.8	43.1	41.6	42.4	42.0	42.9	41.7	43.0	42.2	53.0	51.7	49.6
	0.620	0.570	0.440	0.440	0.430	0.420	0.440	0.430	0.520	0.480	0.440	0.420	0.650	0.650	0.910
	9.77	9.77	8.16	7.18	6.85	6.54	6.37	5.97	5.99	5.94	7.23	6.11	15.63	17.59	13.5
	9.8	9.6	10.2	10.7	11.0	11.6	11.2	12.1	11.1	11.8	10.9	12.3	5.39	5.25	8
	0.170	0.160	0.170	0.170	0.180	0.180	0.180	0.180	0.180	0.170	0.170	0.150	0.110	0.100	0.15
	20.3	20.7	24.0	25.6	26.8	26.5	27.4	27.1	27.1	26.8	26.0	27.4	8.40	7.50	12.1
	5.16	5.38	4.22	3.66	3.62	3.43	3.34	3.07	3.00	3.03	3.75	3.22	7.51	8.29	6.79
	1.49	1.52	1.22	1.11	1.03	0.980	0.950	0.940	0.990	0.880	1.09	0.840	3.18	3.27	3.06
	0.640	0.590	0.570	0.480	0.450	0.410	0.420	0.400	0.540	0.390	0.430	0.430	0.810	0.770	0.570
	0.080	0.069	0.060	0.074	0.062	0.053	0.067	0.083	0.078	0.070	0.073	0.040	0.087	0.078	0.089
	3.76	3.64	4.18	4.12	4.67	4.95	4.93	4.77	4.37	5.49	3.76	5.78	3.04	2.33	3.07
	98.5	98.5	98.5	98.8	99.7	98.2	99.3	98.6	98.4	98.3	98.3	98.9	98.48	98.23	98.82
	19.5	19.3	15.5	15.0	14.9	15.1	14.6	11.7	14.3	13.1	12.5	12.6	27	27.1	23.6
	1350	1390	1660	1770	1800	1560	1950	1580	1810	1830	1730	1020	230	114	590
	93.3	92.7	112	121	117	141	132	140	121	160	110	160	30.7	29.5	49.8
	844	901	1230	1480	1330	2810	1530	2940	1590	3200	1800	4430	116	91.3	300
	92.1	124	183	255	191	970	462	1360	305	1110	530	2270	28.76	33.12	11.80
	24.2	23.7	22.7	19.6	17.8	15.9	17.2	13.6	21.2	14.8	16.1	15.1	35.9	31.5	21
	131	132	107	94.6	78.9	75.2	77.6	67.0	65.5	77.8	87.3	71.3	198	229	150
	15.0	13.2	10.8	11.1	10.7	9.14	10.2	10.4	11.9	10.2	11.5	9.66	17.1	16.4	19.7
	74.6	69.7	63.3	62.7	61.2	52.0	56.4	55.2	70.8	60.2	68.5	56.6	83.9	86.9	89.8
	2.18	1.82	1.70	1.76	1.61	1.42	1.57	1.47	1.86	1.61	1.75	1.45	2.37	2.29	2.65
	110.0	81.9	61.8	73.1	66.5	56.3	63.8	51.7	74.4	62.6	72.6	81.2	230	235	180
	5.49	4.87	4.18	4.63	3.84	3.44	3.83	4.27	4.58	4.03	4.56	3.61	6.41	6.36	6.18
	12.50	11.20	9.62	10.60	9.04	7.75	9.15	9.29	10.50	9.26	10.3	7.91	14.7	14.7	15.3
	1.71	1.46	1.28	1.41	1.22	1.16	1.26	1.20	1.43	1.29	1.38	1.09	1.94	1.91	2.04
	7.61	6.62	5.74	6.23	5.53	5.04	5.63	5.48	6.24	5.30	6.40	4.58	8.31	8.35	9.12
	2.25	1.80	1.57	1.62	1.49	1.31	1.41	1.41	1.64	1.60	1.52	1.40	2.27	2.09	2.63
	0.766	0.731	0.596	0.592	0.566	0.488	0.506	0.519	0.621	0.590	0.517	0.489	0.834	0.850	0.886
	2.50	2.33	1.90	1.92	1.82	1.55	1.74	1.78	2.01	1.77	1.89	1.66	2.66	2.52	3.14
	0.415	0.388	0.304	0.307	0.315	0.264	0.276	0.281	0.345	0.293	0.312	0.280	0.455	0.458	0.537
	2.51	2.34	1.90	1.92	1.86	1.60	1.75	1.67	2.07	1.90	1.90	1.53	2.81	2.68	3.33
	0.598	0.533	0.433	0.431	0.430	0.379	0.385	0.378	0.487	0.433	0.422	0.361	0.652	0.625	0.764
	1.65	1.46	1.21	1.24	1.22	1.07	1.13	0.99	1.35	1.09	1.09	1.05	1.7	1.69	2.01
	0.238	0.217	0.163	0.180	0.174	0.150	0.145	0.157	0.187	0.161	0.156	0.148	0.24	0.23	0.29
	1.53	1.34	1.14	1.09	1.09	0.99	1.05	0.98	1.21	1.10	1.09	1.04	1.53	1.5	1.83
	0.252	0.206	0.149	0.190	0.172	0.154	0.144	0.171	0.194	0.164	0.160	0.153	0.231	0.239	0.275
	1.76	1.75	1.60	1.46	1.41	1.34	1.33	1.32	1.71	1.43	1.64	1.37	1.98	1.95	2.09
	1.47	1.41	1.34	1.21	1.18	0.98	1.01	1.20	1.40	1.20	1.44	1.28	2.06	2.12	1.98
	0.383	0.386	0.335	0.301	0.321	0.299	0.240	0.285	0.356	0.337	0.381	0.319	0.41	0.48	0.41
	3.60	3.64	3.14	3.96	3.04	4.98	3.54	8.73	4.29	12.38	7.31	12.1	4.04	4.20	3.54

References

Allen, M.B., Windley, B.F., Zhang, C., 1993. Palaeozoic collisional tectonics and magmatism of the Chinese Tien Shan, Central Asia. Tectonophysics 220, 89–115.

Ao, S.J., Xiao, W.J., Han, C.M., Mao, Q.G., Zhang, J.E., 2010. Geochronology and geochemistry of early Permian mafic–ultramafic complexes in the Beishan area, Xinjiang, NW China: implications for late Paleozoic tectonic evolution of the southern Altaids. Gondwana Research 18, 466–478.

Arculus, R.J., Powell, R., 1986. Source component mixing in the regions of arc magma generation. Journal of Geophysical Research 91, 5913–5926.

Astis, G.D., Kempton, P.D., Peccerillo, A., Wu, T.W., 2006. Trace element and isotopic variations from Mt. Vulture to Campanian volcanoes: constraints for slab detachment and mantle inflow beneath southern Italy. Contributions to Mineralogy and Petrology 151, 331–351.

Ayers, J.C., Watson, E.B., 1993. Rutile solubility and mobility in supercritical aqueous fluids. Contributions to Mineralogy and Petrology 114, 321–330.

Barnes, S.J., Lightfoot, P.C., 2005. Formation of magmatic nickel sulfide ore deposits and processes affecting their copper and platinum group element contents. Economic Geologists 100, 179–213.

BGMRG (Bureau of Geology and Mineral Resources of Gansu Province), 1989. Regional Geology of Gansu Province, Geological Memoirs, No. 19, Map Scale 1:500000. Geological Publishing House, Beijing (in Chinese).

BGMRXUAR (Bureau of Geology and Mineral Resources of Xinjiang Uygur Autonomous Region), 1993. Regional Geology of Xinjiang Autonomous Region, Geological Memoirs, No. 32, Map Scale 1:500000. Geological Publishing House, Beijing (in Chinese).

Black, L.P., Kamo, S.L., Allen, C.M., Aleinikoff, J.N., Davis, D.S., Korsch, R.J., Foudoulis, C., 2003. TEMORA 1: a new zircon standard for Phanerozoic U–Pb geochronology. Chemical Geology 200, 155–170.

Carroll, A.R., Graham, S.A., Hendrix, M.S., Ying, D., Zhou, D., 1995. Late Paleozoic tectonic amalgamation of northwestern China: sedimentary record of the northern Tarim, northwestern Turpan, and southern Junggar Basins. Geological Society of America Bulletin 107, 571–594.

Chai, G., Naldrett, A.J., 1992. The Jinchuan ultramafic intrusion: cumulate of a high-Mg basaltic magma. Journal of Petrology 33, 277–303.

Charvet, J., Shu, L., Laurent-Charvet, S., 2007. Paleozoic structural and geodynamic evolution of eastern Tianshan (NW China): welding of the Tarim and Junggar plates. Episodes 30, 162–185.

Chen, C.M., Lu, H.F., Jia, D., Cai, D.S., Wu, S.M., 1999. Closing history of the southern Tianshan oceanic basin, western China: an oblique collisional orogeny. Tectonophysics 302, 23–40.

Chen, H.L., Yang, S.F., Dong, C.W., 1997. The discovery of early Permian basic rock belt in Tarim Basin and its tectonic meanings. Geochemica 22, 77–87 (in Chinese with English abstract).

Cole, R.B., Basu, A.R., 1995. Nd–Sr isotopic geochemistry and tectonics of ridge subduction and middle Cenozoic volcanism in western California. Geological Society of America Bulletin 107, 167–179.

Cole, R.B., Stewart, B.W., 2007. Continental margin volcanism at sites of spreading ridge subduction: examples from southern Alaska and western California. Tectonophysics 464, 118–136.

Compston, W., Williams, I.S., Kirschvink, J.L., 1992. Zircon U–Pb ages for the early Cambrian timescale. Journal of the Geological Society 149, 171–184.

Crawford, A.J., Berry, R.F., 1992. Tectonic implications of Late Proterozoic–Early Palaeozoic igneous rock associations in western Tasmania. Tectonophysics 214, 7–56.

Crawford, A.J., Falloon, T.J., Eggins, S., 1987. The origin of island arc high alumina basalts. Contributions to Mineralogy and Petrology 97, 417–430.

D'Orazio, M., Innocenti, F., Manetti, P., Tamponi, M., Tonarini, S., Gonzàlez-Ferràn, O., Lahsen, A., Omarini, R., 2001. The Quaternary calc-alkaline volcanism of the Patagonian Andes close to the Chile triple junction: geochemistry and petrogenesis of volcanic rocks from the Cay and Maca volcanoes (~45° S, Chile). Journal of South American Earth Sciences 16, 219–242.

Davies, J.H., von Blanckenburg, F., 1995. Slab breakoff: a model of lithosphere detachment and its test in the magmatism and deformation of collisional orogens. Earth and Planetary Science Letters 129, 85–102.

Dobretsov, N.L., 2003. Evolutions of structures of the Urals, Kazakhstan, Tien Shan, and Altay–Sayan region within the Ural–Mongolian fold belt. Russian Geology and Geophysics 44, 5–27.

Florisbal, L.M., Bitencourt, M.F., Nardi, L.V.S., Conceição, R.V., 2009. Early post-collisional granitic and coeval mafic magmatism of medium- to high-K tholeiitic affinity within the Neoproterozoic Southern Brazilian Shear Belt. Precambrian Research 175, 135–148.

Gorring, M., Singer, B., Gowers, J., Kay, S.M., 2003. Plio-Pleistocene basalts from the Meseta del Lago Buenos Aires, Argentina: evidence for asthenosphere–lithosphere interactions during slab window magmatism. Chemical Geology 193, 215–235.

Green, D.H., Falloon, T.J., 1998. Pyrolite: a Ringwood concept and its current expression. In: Jackson, I. (Ed.), The Earth's Mantle: Composition, Structure, and Evolution. Cambridge University Press, London, pp. 311–380.

Guo, Z.J., Shi, H.Y., Zhang, Z.C., Zhang, J.J., 2006. The tectonic evolution of the south Tianshan paleo-oceanic crust inferred from the spreading structures and Ar–Ar dating of the Hongliuhe ophiolite, NW China. Acta Petrologica Sinica 22, 95–102 (in Chinese with English abstract).

Guo, J., Shu, L.S., Charvet, J., Laurent, C.S., Sun, S.W., 2002. Geochemical features of the two early Paleozoic ophiolitic zones and volcanic rocks in the central-southern Tianshan Region, Xinjiang. Chinese Journal of Geochemistry 21, 308–321.

Han, B.F., Ji, J.Q., Song, B., Chen, L.H., Li, Z.H., 2004. Zircon SHRIMP U–Pb age and geology of Kalatongke–Huangshan mafic–ultramafic complex, Xinjiang. China. Chinese Science Bulletin 49, 2324–2328 (in Chinese with English abstract).

Han, B.F., Wang, S.G., Jahn, B.M., Hong, D.W., Kagami, H., Sun, Y.L., 1997. Depleted mantle source for the Ulungur River A-type granites from North Xinjiang, China: geochemistry and Nd–Sr isotopic evidence, and implications for the Phanerozoic crustal growth. Chemical Geology 138, 135–159.

Han, C.M., Xiao, W.J., Zhao, G.C., Ao, S.J., Zhang, J.E., Qu, W.J., Du, A.D., 2010. In-situ U–Pb, Hf and Re–Os isotopic analyses of the Xiangshan Ni–Cu–Co deposit in Eastern Tianshan (Xinjiang), Central Asia Orogenic Belt: constraints on the timing and genesis of the mineralization. Lithos 120, 540–567.

Hawkesworth, C.J., Powell, M., 1980. Magma genesis in the lesser Antilles Island arc. Earth and Planetary Science Letters 51, 297–308.

He, G.Q., Li, M.S., Liu, D.Q., Zhou, N.H., 1994. Palaeozoic Crustal Evolution and Mineralization in Xinjiang of China. Xinjiang People's Publication House, Urumqi. (in Chinese with English abstract).

Hirose, K., Kawamoto, T., 1995. Hydrous partial melting of lherzolite at 1 Gpa: the effect of H_2O on the genesis of basaltic magmas. Earth and Planetary Science Letters 133, 463–473.

Hu, A.Q., Jahn, B.M., Zhang, G., Chen, Y., Zhang, Q., 2000. Crustal evolution and Phanerozoic crustal growth in northern Xinjiang: Nd isotopic evidence. Part I. Isotopic characterization of basement rocks. Tectonophysics 328, 15–51.

Jahn, B.M., Windley, B., Natal'in, B., Dobretsov, N., 2004. Phanerozoic continental growth in Central Asia. Journal of Asian Earth Sciences 23, 599–603.

Jahn, B.M., Wu, F., Chen, B., 2000. Granitoids of the Central Asian orogenic belt and continental growth in the Phanerozoic. Transactions of the Royal Society of Edinburgh: Earth Sciences 91, 181–193.

Jiang, C.Y., Cheng, S.L., Ye, S.F., Xia, M.Z., Jiang, H.B., Dai, Y.C., 2006. Lithogeochemistry and petrogenesis of Zhongposhanbei mafic rock body, at Beishan region, Xinjiang. Acta Petrologica Sinica 22, 115–126 (in Chinese with English abstract).

Jiang, C.Y., Zhang, P.B., Lu, D.R., Bai, K.Y., Wang, Y.P., Tang, S.H., Wang, J.H., Yang, C., 2004. Petrology, geochemistry and petrogenesis of the Kalpin basalts and their Nd, Sr and Pb isotopic compositions. Geological Review 50, 492–500 (in Chinese with English abstract).

Johnson, M.C., Plank, T., 1999. Dehydration and melting experiments constrain the fate of subducted sediments. Geochemistry, Geophysics, Geosystems 1, 1007. doi:10.1029/1999GC000014.

Keays, R.R., Lightfoot, P.C., 2007. Siderophile and chalcophile metal variations in Tertiary picrites and basalts from West Greenland with implications for the sulphide saturation history of continental flood basalt magmas. Mineral Deposita 42, 319–336.

Keays, R.R., Lightfoot, P.C., 2010. Crustal sulfur is required to form magmatic Ni–Cu sulfide deposits: evidence from chalcophile element signatures of Siberian and Deccan Trap basalts. Mineralium Deposita 45, 241–257.

Kelemen, P.B., Rilling, J.L., Parmentier, E.M., Mehl, L., Hacker, B.R., 2003. Thermal structure due to solid-state flow in the mantle wedges beneath arcs. Geophysical Monograph 138, 293–311.

Keppler, H., 1996. Constraints from partitioning experiments on the composition of subduction-zone fluids. Nature 380, 237–240.

Keskin, M., 2003. Magma generation by slab steepening and breakoff beneath a subduction–accretion complex: an alternative model for collision-related volcanism in Eastern Anatolia, Turkey. Geophysical Research Letters 30. doi:10.1029/2003GL018019.

Kheraskova, T.N., Didenko, A.N., Bush, V.A., Volozh, Y.A., 2003. The Vendian–Early Paleozoic history of the continental margin of Eastern Paleogondwana, Paleoasian Ocean, and Central Asian Fold belt. Russian Journal of Earth Sciences 5, 165–184.

Krogh, T.E., 1973. A low contamination method for the hydrothermal decomposition of zircon and extraction of U and Pb for isotope age determination. Geochimica et Cosmochimica Acta 37, 485–494.

Laurent-Charvet, S., Charvet, J., Monie, P., Shu, L., 2003. Late Paleozoic strike-slip shear zones in eastern central Asia (NW China): new structural and geochronological data. Tectonics 22. doi:10.1029/2001TC90104.

Li, H.Q., Chen, F.W., Mei, Y.P., Wu, H., Chen, S.L., Yang, J.Q., Dai, Y.C., 2006. Isotopic ages of No.1 intrusive body in Pobei mafic–ultramafic belt of Xinjiang and their geological significance. Mineral Deposits 25, 463–469 (in Chinese with English abstract).

Li, Z.L., Yang, S.F., Chcn, H.L., Langmuir, C.H., Yu, X., Lin, X.B., Li, Y.Q., 2008. Chronology and geochemistry of Taxinan basalts from the Tarim basin: evidence for Permian plume magmatism. Acta Petrologica Sinica 24, 959–970 (in Chinese with English abstract).

Lin, W., Faure, M., Shi, Y.H., Wang, Q.C., Li, Z., 2009. Palaeozoic tectonics of the south-western Chinese Tianshan: new insights from a structural study of the high-pressure/low-temperature metamorphic belt. International Journal of Earth Sciences 98, 1259–1274.

Liu, X.C., Chen, B.L., Jahn, B., Wu, G.G., Liu, Y.S., 2011. Early Paleozoic (ca. 465 Ma) eclogites from Beishan (NW China) and their bearing on the tectonic evolution of the southern Central Asian Orogenic Belt. Journal of Asian Earth Sciences 42, 715–731.

Lu, S.N., Li, H.K., Li, H.M., Song, B., Wang, S.Y., Zhou, H.Y., Chen, Z.H., 2003. U–Pb isotopic ages and their significance of alkaline granite in southern margin of the north China Craton. Geological Bulletin of China 22, 762–768 (in Chinese with English abstract).

Ludwig, K.R., 1994. Isoplot: a plotting and regression program for radiogenic isotope data. US Geological Survey, Open-file Report, Version 2.75, pp. 41–45.

Ludwig, K.R., 2001a. Squid 1.02. A User Manual. Berkeley Geochronological Center Special Publication, Berkeley, pp. 1–219.

Ludwig, K.R., 2001b. Using Isoplot/EX, version 2.49. A Geochronological Toolkit for Microsoft Excel. Berkeley Geochronological Center Special Publication, Berkeley, pp. 1–55.

Maier, W.D., Barnes, S.-J., Chinyepi, G., Barton Jr., J.M., Eglington, B., Setshedi, I., 2008. The composition of magmatic Ni–Cu–(PGE) sulfide deposits in the Tati and Selebi–Phikwe belts of eastern Botswana. Mineralium Deposita 43, 37–60.

Mao, J.W., Pirajno, F., Zhang, Z.H., Chai, F.M., Wu, H., Chen, S.P., Cheng, S.L., Yang, J.M., Zhang, C.Q., 2008. A review of the Cu–Ni sulphide deposits in the Chinese Tianshan and Altay orogens (Xinjiang Autonomous Region, NW China): principal characteristics and ore-forming processes. Journal of Asian Earth Sciences 32, 184–203.

Martinez, F., Taylor, B., 2002. Mantle wedge control on back-arc crustal accretion. Nature 416, 417–420.

Miller, J.S., Glazner, A.F., Farmer, G.L., Suayah, I.B., Keith, L.A., 2000. A Sr, Nd, Pb isotopic study of mantle domains and crustal structure from Miocene volcanic rocks in the Mojave Desert, California. Geological Society of America Bulletin 112, 1264–1279.

Moghadam, H.S., Stern, R.J., Rahgoshay, M., 2010. The Dehshir ophiolite (central Iran): geochemical constraints on the origin and evolution of the Inner Zagros ophiolite belt. Geological Society of America Bulletin 122, 1516–1547.

Mossakovsky, A.A., Ruzhentsev, S.V., Samygin, S.G., Kheraskova, T.N., 1993. The Central Asian fold belt: geodynamic evolution and formation history. Geotectonics 26, 455–473.

Naldrett, A.J., 1999. World-class Ni–Cu–PGE deposits: key factors in their genesis. Mineralium Deposita 34, 227–240.

Nasdala, L., Hofmeister, W., Norberg, N., Martinson, J.M., Corfu, F., Dörr, W., Kamo, S.L., Kennedy, A.K., Kronz, A., Reiners, P.W., Frei, D., Kosler, J., Wan, Y.S., Götze, J., Hager, T., Kröner, A., Valley, J.W., 2008. Zircon M257 — a homogeneous natural reference material for the ion microprobe U–Pb analysis of zircon. Geostandards and Geoanalytical Research 32, 247–265.

Paktunc, A.D., 1990. Comparative geochemistry of platinum-group elements of nickel–copper sulfide occurrences associated with mafic–ultramafic intrusions in the Appalachian orogen. Journal of Geochemical Exploration 37, 101–111.

Pearce, J.A., Peate, D.W., 1995. Tectonic implications of the composition of volcanic arc magmas. Annual Reviews of Earth and Planetary Sciences 23, 251–285.

Pearce, J.A., Stern, R.J., Bloomer, S.H., Fryer, P., 2005. Geochemical mapping of the Mariana arc-basin system: implications for the nature and distribution of subduction components. Geochemistry, Geophysics, Geosystems 6, Q07006. doi:10.1029/2004GC000895.

Pina, R., Lunar, R., Ortega, L., Gevilla, F., Alapieti, T., Martinez, C., 2006. Petrology and geochemistry of mafic–ultramafic fragments from the Aguablanca Ni–Cu ore breccia, southwest Spain. Economic Geology 101, 865–881.

Pirajno, F., Mao, J.W., Zhang, Z.C., Zhang, Z.H., Chai, F.M., 2008. The association of mafic–ultramafic intrusions and A-type magmatism in the Tianshan and Altay orogens, NW China: implications for geodynamic evolution and potential for the discovery of new ore deposits. Journal of Asian Earth Sciences 32, 165–183.

Qi, L., Hu, J., Conrad, G., 2000. Determination of trace elements in granites by inductively coupled plasma mass spectrometry. Talanta 51, 507–513.

Qin, K.Z., Su, B.X., Sakyi, P.A., Tang, D.M., Li, X.H., Sun, H., Xiao, Q.H., Liu, P.P., 2011. SIMS zircon U–Pb geochronology and Sr–Nd isotopes of Ni–Cu-bearing mafic–ultramafic intrusions in Eastern Thanshan and Beishan in correlation with flood basalts in Tarim Basin (NW China): constraints on a ca. 280 Ma mantle plume. American Journal of Science 311. doi:10.2475/04.2011.00.

Qin, K.Z., Zhang, L.C., Xiao, W.J., Xu, X.W., Yan, Z., Mao, J.W., 2003. Overview of major Au, Cu, Ni and Fe deposits and metallogenic evolution of the eastern Tianshan Mountains, Northwestern China. In: Mao, J.W., Goldfarb, R., Seltmann, R., Wang, D.H., Xiao, W.J., Hart, C. (Eds.), Tectonic Evolution and Metallogeny of the Chinese Altay and Tianshan. Natural History Museum, London, pp. 227–249.

Ripley, E.M., Lightfoot, P.C., Li, C.S., Elswick, E.R., 2003. Sulfur isotopic studies of continental flood basalts in the Noril'sk region: implications for the association between lavas and ore-bearing intrusions. Geochimica et Cosmochimica Acta 67, 2805–2817.

Roeder, P.L., Emslie, R.F., 1970. Olivine-liquid equilibrium. Contributions to Mineralogy and Petrology 29, 275–289.

Rudnick, R.L., Gao, S., 2003. Composition of the continental crust. In: Rudnick, R.L. (Ed.), Treatise on Geochemistry. Elsevier Science Ltd, Amsterdam, pp. 1–64.

San, J.Z., Qin, K.Z., Tang, Z.L., Tang, D.M., Su, B.X., Sun, H., Xiao, Q.H., Liu, P.P., 2010. Precise zircon U–Pb age dating of two mafic–ultramafic complexes at Tulargen large Cu–Ni district and its geological implications. Acta Petrologica Sinica 26, 3027–3035 (in Chinese with English abstract).

Sengör, A.M.C., Natal'In, B.A., 1996. Turkic-type orogeny and its role in the making of the continental crust. Annual Reviews of Earth and Planetary Sciences 24, 263–337.

Sengör, A.M.C., Natal'In, B.A., Burtman, U.S., 1993. Evolution of the Altaid tectonic collage and Palaeozoic crustal growth in Eurasia. Nature 364, 299–307.

Song, X.Y., Li, X.R., 2009. Geochemistry of the Kalatongke Ni–Cu–(PGE) sulfide deposit, NW China: implications for the formation of magmatic sulfide mineralization in a postcollisional environment. Mineralium Deposita 44, 303–327.

Song, X.Y., Xie, W., Deng, Y.F., Crawford, A.J., Zheng, W.Q., Zhou, G.F., Deng, G., Cheng, S.L., Li, J., 2011. Slab break-off and the formation of Permian mafic–ultramafic intrusions in southern margin of Central Asian Orogenic Belt, Xinjiang, NW China. Lithos 127, 128–143.

Song, B., Zhang, Y.H., Wan, Y.S., Jian, P., 2002. The SHRIMP sample manufacture, test and explanation of some phenomena for the zircon. Geological Review 48, 26–30 (in Chinese with English abstract).

Stern, C.R., Kilian, R., 1996. Role of the subducted slab, mantle wedge and continental crust in the generation of adakites from the Andean Austral Volcanic Zone. Contributions to Mineralogy and Petrology 123, 263–281.

Stolz, A.J., Jochum, K.P., Spettel, B., Hafmann, A.W., 1996. Fluid- and melt-related enrichment in the subarc mantle: evidence from Nb/Ta variations in island-arc basalts. Geology 24, 587–590.

Su, B.X., Qin, K.Z., Sakyi, P.A., Li, X.H., Yang, Y.H., Sun, H., Tang, D.M., Liu, P.P., Xiao, Q.H., Malaviarachchi, S.P.K., 2011. U–Pb ages and Hf–O isotopes of zircons from Late Paleozoic mafic–ultramafic units in the southern Central Asian Orogenic Belt: tectonic implications and evidence for an Early-Permian mantle plume. Gondwana Research 20, 516–531.

Su, B.X., Qin, K.Z., Sakyi, P.A., Malaviarachchi, S.P.K., Liu, P.P., Tang, D.M., Xiao, Q.H., Sun, H., Ma, Y.G., Mao, Q., 2012. Occurrence of an Alaskan-type complex in the Middle Tianshan Massif, Central Asian Orogenic Belt: inferences from petrological and mineralogical studies. International Geology Review 54, 249–269.

Su, B.X., Qin, K.Z., Sakyi, P.A., Tang, D.M., Liu, P.P., Malaviarachchi, S.P.K., Xiao, Q.H., Sun, H., 2010. Geochronologic–petrochemical studies of the Hongshishan mafic–ultramafic intrusion, Beishan area, Xinjiang (NWChina): petrogenesis and tectonic implications. International Geology Review. doi:10.1080/00206814.2010.543011.

Su, B.X., Qin, K.Z., Sun, H., Wang, H., 2010. Geochronological, petrological, mineralogical and geochemical studies of the Xuanwoling mafic–ultramafic intrusion in the Beishan area, Xinjiang. Acta Petrologica Sinica 26, 3283–3294 (in Chinese with English abstract).

Sun, S.S., McDonough, W.F., 1989. Chemical and isotopic systematics of oceanic basalts: implications for mantle composition and processes. In: Saunders, A.D., Norry, M.J. (Eds.), Magmatism in the Ocean Basins. Geological Society Special Publications, London, pp. 313–345.

Takazawa, E., Frey, F.A., Shimizu, N., Obtata, M., 2000. Whole rock compositional variations in an upper mantle peridotite (Horoman, Hokkaido, Japan): are they consistent with a partial melting process? Geochimica et Cosmochimica Acta 64, 695–716.

Tang, K., 1990. Tectonic development of Paleozoic fold belts at the north margin of the Sino-Korean craton. Tectonics 9, 249–260.

Tang, D.M., Qin, K.Z., Sun, H., Su, B.X., Xiao, Q.H., Cheng, S.L., Li, J., 2009. Lithological, chronological and geochemical characteristics of Tianyu Cu–Ni deposit: constraints on source and genesis of mafic–ultramafic intrusions in eastern Xinjiang. Acta petrologica Sinica 25, 817–831 (in Chinese with English abstract).

Tang, K., Yan, Z., 1993. Regional metamorphism and tectonic evolution of the Inner Mongolian suture zone. Journal of Metamorphic Geology 11, 511–522.

Thorkelson, D.J., 1996. Subduction of diverging plates and the principles of slab window formation. Tectonophysics 255, 47–63.

Tornos, F., Casquet, C., Galindo, C., Velasco, F., Canales, A., 2001. A new style of Ni–Cu mineralization related to magmatic breccia pipes in a transpressional magmatic arc, Aguablanca, Spain. Mineralium Deposita 36, 700–706.

Wang, B., Faure, M., Shu, L.S., de Jong, K., Charvet, J., Cluzel, D., Jahn, B.M., Chen, Y., Ruffet, G., 2010. Structural and geochronological study of high-pressure metamorphic rocks in the Kekesu section (Northwestern China): implications for the late Paleozoic tectonics of the southern Tianshan. Journal of Geology 118, 59–77.

Williams, I.S., 1998. U–Th–Pb geochronology by ion microprobe. Reviews in Economic Geology 7, 1–35.

Wilson, M., 1989. Igneous Petrogenesis. Unwin Hyman, London.

Windley, B.F., Alexeiev, D., Xiao, W.J., Kröner, A., Badarch, G., 2007. Tectonic models for accretion of the Central Asian Orogenic Belt. Journal of the Geological Society 164, 31–47.

Windley, B.F., Allen, M.B., Zhang, C., Zhao, Z.Y., Wang, G.R., 1990. Paleozoic accretion and Cenozoic redeformation of the Chinese Tien Shan Range, Central Asia. Geology 18, 128–131.

Wood, D.A., 1980. The application of a Th–Hf–Ta diagram to problems of tectonomagmatic classification and to establishing the nature of crustal contamination of basaltic lavas of the British Tertiary volcanic province. Earth and Planetary Science Letters 50, 11–30.

Wu, H., Li, H.Q., Mo, X.H., Chen, F.W., Lu, Y.F., Mei, Y.P., Deng, G., 2005. Age of the Baishiquan mafic–ultramafic complex, Hami, Xinjiang and its geological significance. Acta Geologica Sinica 79, 498–502 (in Chinese with English abstract).

Xiao, W.J., Han, C.M., Yuan, C., Sun, M., Lin, S.F., Chen, H.L., Li, Z.L., Li, J.L., Sun, S., 2008. Middle Cambrian to Permian subduction-related accretionary orogenesis of Northern Xinjiang, NW China: implications for the tectonic evolution of Central Asia. Journal of Asian Earth Sciences 32, 102–117.

Xiao, W.J., Mao, Q.G., Windley, B.F., Han, C.M., Qu, J.F., Zhang, J.E., Ao, S.J., Guo, Q.Q., Ckeven, N.R., Lin, S.F., Shan, Y.H., Li, J.L., 2010. Paleozoic multiple accretionary and collisional processes of the Beishan Orogenic Collage. American Journal of Science 310, 1553–1594.

Xiao, W.J., Zhang, L.C., Qin, K.Z., Sun, S., Li, J.L., 2004. Paleozoic accretionary and collisional tectonics of the Eastern Tianshan (China): implications for the continental growth of Central Asia. American Journal of Science 304, 370–395.

Xie, W., Song, X.Y., Nie, X.Y., Cheng, S.L., 2011. Features of the mantle source and tectonic setting of the Poshi Ni–Cu sulfide-bearing intrusion, Xinjiang, China. Earth Science Frontiers 18, 189–200 (in Chinese with English abstract).

Xu, Z., Han, B.F., Ren, R., Zhou, Y.Z., Zhang, L., Chen, J.F., Su, L., Li, X.H., Liu, D.Y., 2012. Ultramafic–mafic mélange, island arc and post-collisional intrusions in the Mayile Mountain, West Junggar, China: implications for Paleozoic intra-oceanic subduction–accretion process. Lithos 132–133, 141–161.

Yang, S.F., Li, Z.L., Chen, H.L., Chen, W., Yu, X., 2006. 40Ar–39Ar dating of basalts from Tarim Basin, NW China and its implication to a Permian thermal tectonic event. Journal of Zhejiang University. Science 7 (Suppl. II), 320–324.

Zhang, Y.Y., Dostal, J.D., Zhao, Z.H., Liu, C., Guo, Z.J., 2011. Geochronology, geochemistry and petrogenesis of mafic and ultramafic rocks from southern Beishan area, NW China: implications for crust–mantle interaction. Gondwana Research. doi:10.1016/j.gr.2011.03.008.

Zhang, Y.Y., Guo, Z.J., 2008. Accurate constraint on formation and emplacement age of Hongliuhe ophiolite, boundary region between Xinjiang and Gansu provinces and its tectonic implications. Acta Petrologica Sinica 24, 803–809 (in Chinese with English abstract).

Zhang, C.L., Li, X.H., Li, Z.X., Ye, H.M., Li, C.N., 2008. A Permian layered intrusive complex in the Western Tarim Block, Northwestern China: product of a ca. 275-Ma mantle plume? Journal of Geology 116, 269–287.

Zhang, Z.C., Mao, J.W., Chai, F.M., Yan, S.H., Chen, B.L., 2009. Geochemistry of the Permian Kalatongke mafic intrusions, Northern Xinjiang, northwest China: implications

for the genesis of magmatic Ni–Cu sulfide deposits. Economic Geology 104, 185–203.

Zhang, Z.C., Yan, S.H., Chen, B.L., He, L.X., He, Y.S., Zhou, G., Chai, F.M., 2006. Sr, Nd, O isotope geochemistry of the mafic–ultramafic complexes in the south margin of Altay orogenic belt and discussion on their sources. Geological Review 52, 38–42 (in Chinese with English abstract).

Zhou, M.F., Lesher, C.M., Yang, Z.X., Li, J.W., Sun, M., 2004. Geochemistry and petrogenesis of 270 Ma Ni–Cu–(PGE) sulfide-bearing mafic intrusions in the Huangshan District, eastern Xinjiang, northwest China: implications for the tectonic evolution of the Central Asian orogenic belt. Chemical Geology 209, 233–257.

Zhou, M.F., Zhao, J.H., Jiang, C.Y., Gao, J.F., Wang, W., Yang, S.H., 2009. OIB-like, heterogeneous mantle sources of Permian basaltic magmatism in the western Tarim Basin, NW China: implications for a possible Permian large igneous province. Lithos 113, 583–594.

Zimmer, M.M., Plank, T., Hauri, E.H., Yogodzinski, G.M., Stelling, P., Larsen, J., Singer, B., Jicha, B., Mandeville, C., Nye, C.J., 2010. The role of water in generating the calc-alkaline trend: new volatile data for Aleutian magmas and a new tholeiitic index. Journal of Petrology 51, 2411–2444.

Zindler, A., Hart, S., 1986. Chemical geodynamics. Annual Review of Earth and Planetary Sciences 14, 493–571.